SANDIA REPORT
SAND2013-5112
Unlimited Release
Printed June 2013

Simulation of Primary Fuel Atomization Processes at Subcritical Pressures

Marco Arienti

Prepared by
Sandia National Laboratories
Albuquerque, New Mexico 87185 and Livermore, California 94550

Sandia National Laboratories is a multi-program laboratory managed and operated by Sandia Corporation,
a wholly owned subsidiary of Lockheed Martin Corporation, for the U.S. Department of Energy's
National Nuclear Security Administration under contract DE-AC04-94AL85000.

Approved for public release; further dissemination unlimited.

Sandia National Laboratories

Issued by Sandia National Laboratories, operated for the United States Department of Energy by Sandia Corporation.

NOTICE: This report was prepared as an account of work sponsored by an agency of the United States Government. Neither the United States Government, nor any agency thereof, nor any of their employees, nor any of their contractors, subcontractors, or their employees, make any warranty, express or implied, or assume any legal liability or responsibility for the accuracy, completeness, or usefulness of any information, apparatus, product, or process disclosed, or represent that its use would not infringe privately owned rights. Reference herein to any specific commercial product, process, or service by trade name, trademark, manufacturer, or otherwise, does not necessarily constitute or imply its endorsement, recommendation, or favoring by the United States Government, any agency thereof, or any of their contractors or subcontractors. The views and opinions expressed herein do not necessarily state or reflect those of the United States Government, any agency thereof, or any of their contractors.

Printed in the United States of America. This report has been reproduced directly from the best available copy.

Available to DOE and DOE contractors from
U.S. Department of Energy
Office of Scientific and Technical Information
P.O. Box 62
Oak Ridge, TN 37831

Telephone: (865) 576-8401
Facsimile: (865) 576-5728
E-Mail: reports@adonis.osti.gov
Online ordering: http://www.osti.gov/bridge

Available to the public from
U.S. Department of Commerce
National Technical Information Service
5285 Port Royal Rd.
Springfield, VA 22161

Telephone: (800) 553-6847
Facsimile: (703) 605-6900
E-Mail: orders@ntis.fedworld.gov
Online order: http://www.ntis.gov/help/ordermethods.asp?loc=7-4-0#online

SAND2013-5112
Unlimited Release
Printed June 2013

Simulation of Primary Fuel Atomization Processes at Subcritical Pressures

Marco Arienti
Thermal/Fluid Science and Engineering
Sandia National Laboratories
7011 East Avenue,
Livermore, CA 94550 MS 9052

Abstract

This report documents results from an LDRD project for the first-principles simulation of the early stages of spray formation (primary atomization). The first part describes a Cartesian embedded-wall method for the calculation of flow internal to a real injector in a fully coupled primary calculation. The second part describes the extension to an all-velocity formulation by introducing a momentum-conservative semi-Lagrangian advection and by adding a compressible term in the Poisson's equation. Accompanying the description of the new algorithms are verification tests for simple two-phase problems in the presence of a solid interface; a validation study for a scaled-up multi-hole Diesel injector; and demonstration calculations for the closing and opening transients of a single-hole injector and for the high-pressure injection of liquid fuel at supersonic velocity.

ACKNOWLEDGMENTS

A big thanks to Sarah Scott (8365) for her relentless effort at generating the meshes for all the injectors.

CONTENTS

FIGURES

TABLES

1 INTRODUCTION

Radical changes in engine design to meet high efficiency and low emission demands require better predictive computational capabilities. The sophisticated combustion codes that have been developed at Sandia must be provided with the correct boundary conditions – namely the distribution of fuel spray near injection if direct liquid injection is the mechanism to deliver fuel to the combustion chamber. Direct observation of fuel atomization into drops is difficult: nozzles are typically about a millimeter long and a fraction of a millimeter in diameter, and the flow moves at speeds of the order of several hundred meters per second. Multiple scattering renders much of the optical diagnostics of limited use near the injector. The fact that the fuel can partially vaporize in the nozzle adds another level of complexity. Overall, the understanding of the physics that controls the fuel/air distribution of many combustion devices, particularly at high pressure, is quite limited.

The main objective of this project is to predict the spatial spray distribution from high-pressure injection. Throughout this report the liquid phase will be considered sub-critical, therefore with a distinguishable gas-liquid interface. A recent review of modelling techniques for fuel injectors [1] indicates that a direct numerical simulation (DNS) of a two-phase flow with sharp and time-resolved liquid-gas interface, while computationally expensive, is feasible thanks to the small volume where primary atomization takes place. The main challenge of this project was then to select an existing computer code for free-surface flow and to augment it with the capability to handle complex, possibly moving, injector geometries and high-pressure states of the fuel.

The computer code CLSVOF (Combined Level Set Volume Of Fluid) was selected as the platform best suited for further development. CLSVOF is a finite-volume, pressure-based, multigrid solver for the incompressible, multi-fluid Navier-Stokes equations [2]. The distinguishing feature of the code is the CLSVOF technique that is used to capture the gas-liquid interface in time-resolved manner. The solver can also access a coarse-grained, grid-adaptive, parallel, computational environment thanks to the library Boxlib, developed at the Berkeley Lab to enable a common platform for high-performance computing [3].

The application of CLSVOF to fluid dynamic problems relevant to fuel injection in aero- and rocket engines [4] was initiated by the author of this report and carried out in collaboration with the code main developer, Professor Mark Sussman from Florida State University [5]. CLSVOF has been validated in fuel atomization calculations with large liquid/gas density ratios (up to 1000:1) and large Weber numbers (up to 200). Reference [6] provides a good description of the capability of the code in the early phase of this project. A like-on-like jet impingement simulation for low, moderate, and high injection velocities was compared to experimental data, showing that the salient features of the spray fan breakup and ligament frequencies were in overall agreement with both trends and magnitudes reported in the experiment. Particularly, the spray droplets distribution converged to the phase Doppler particle analyser data as the grid density was increased. These simulations represent an almost unique instance of primary atomization calculation executed without subgrid models on the scale and at the conditions of an actual experiment and directly validated with spray distribution measurements. One of such validation studies was carried out as a task of the LDRD.

The first part of this report describes a new embedded wall method for a Cartesian mesh. This method was chosen as the least intrusive approach to CLSVOF to retain the superior efficiency of interface capturing on a Cartesian mesh. The embedded wall method is designed so that the fluid dynamics solver can operate on each grid block unaware of the existence of a solid body within it: this approach requires the correct setting of face values for the computational cells that are traversed by the solid boundary.

The second part of the report briefly highlights the two modifications in the code that enable the extension of the incompressible pressure solver to an all-velocity formulation: a momentum-conservative semi-Lagrangian advection; and the addition of a compressible term in the Poisson's equation. Density advection is carried out for each phase separately. Moreover, a simulation can be set up by choosing whether each material is compressible (and in that case, what its equation of state is), or incompressible. This arrangement is convenient in many fuel injection simulations when only the gas phase needs to be treated as compressible, while signal transmission in the liquid phase can be ignored. A demonstration of fuel injected at a velocity larger than the sound speed of the gas phase – causing a leading oblique shock followed by several weaker acoustic waves in the gas phase – illustrates this point. The time evolution of the transient fuel spray from the simulation is compared with synchrotron x-radiography, showing good qualitative agreement in the strength of the leading shock.

As noted in the Conclusion, at the end of this project not all the validation cases of the incompressible solver have been repeated for the compressible version: doing so will be a priority for future projects. Funding opportunities, some of which have already materialized, will leverage on the capabilities developed in this LDRD.

2 AN EMBEDDED LEVEL SET METHOD FOR SHARP-INTERFACE MULTIPHASE SIMULATIONS OF DIESEL INJECTORS[1]

2.1 Abstract

We propose a comprehensive approach for treating complex wall boundaries in two-phase, free-surface flow simulations on a Cartesian adaptive grid. The external liquid-gas interface is handled by the well-known combined level-set volume-of-fluid (CLSVOF) method. The new element is the coupling with the wall boundary representation obtained using a second level-set function. The merging and separation of multiple solid bodies can be easily accommodated in this framework. The no-slip boundary condition at the walls is enforced by properly populating the ghost cells of a narrow band inside the solid body with a simple and numerically robust treatment for the contact line. Verification tests with grid convergence analysis are presented for a stationary/oscillating body in single-phase flow and for a drop on an inclined plane. Two examples demonstrate the suitability of the proposed approach to study liquid injection. The first is a validation study with data from a scaled-up, transparent Diesel injector, to demonstrate how the seamless calculation of internal flow and jet primary atomization can be accomplished. The second is a demonstration of transient atomization response to a fully three-dimensional needle displacement of the injector.

2.2 Introduction

There are many free-surface flows that also require the management of complex boundary walls. One example is the process of spray formation from liquid injection. The simulation from first principles of spray atomization requires a non-trivial model of the injector in order to correctly define the boundary conditions of the calculation. The method for time-resolved interface capturing called CLSVOF (combined level-set volume-of-fluid) was applied, under various implementations, to model bubble and drop dynamics in viscous and viscoelastic environments [2, 7 ,8], ship waves [9], and underwater explosions [10]. Validation was carried out for sprays formed from jets subject to gas crossflow [11] or impinging on each other [12], in the latter case with excellent agreement with the statistics derived from experimental measurements.

Under the assumption that internal flow characteristics had limited effects on primary atomization, a simple plug flow velocity profile was assigned as a boundary condition in Arienti et al. (2013). A more realistic inflow, via correlated random velocities with assumed length scale and turbulence intensity, was generated at the orifice exit of a jet injection simulation by Ménard, et al. [13], but very few studies have attempted to include the inflow turbulent conditions that result from the actual injector geometry. Notably, in the simulation of jet injection in gas crossflow by Herrmann [14], the injector was modeled as a short pipe tapering into a flush

---

[1] The content of this chapter was submitted to the International Journal of Multiphase Flow on Jan. 19th 2013. It is in the process of being re-submitted with modifications that address the reviewers' comments.

orifice. A single-phase, pre-computed large eddy simulation of pipe flow was stored as a time sequence of the pre-taper portion of the injector in the subsequent two-phase simulation.

In this paper we develop a general approach to include the whole injector geometry in a primary atomization simulation. This is accomplished by introducing a second level set function to represent the injector's walls in addition to the level set used to capture the gas-liquid interface. This approach is a valid alternative to boundary-fitted methods, where issues of grid deformation, re-generation and interpolation at each physical timestep can become critical in the case of moving walls. The solution we propose is to let solid boundaries and phase interfaces have unrestricted motion across underlying fixed grid lines. Not being constrained by wall shapes, the choice of the computational grid can be optimized for free-surface flow by selecting an isotropic and equispaced – Cartesian – grid.

The most delicate and time consuming operation with Cartesian methods becomes the intersection of the solid body with the regular grid. This has prompted the development of several efficient algorithms for cut cells (for instance, in [15]). Motion and deformation of the solid body, possibly governed by a separate solver, as in [16], can still be fully coupled to the flow simulation. However, since cells cut by the solid wall can be arbitrarily small, explicit update schemes become overly restrictive for time-dependent problems, requiring either to extend the difference stencil of the spatial terms [17] or to use a cell-merging approach [18].

With a moving or deforming solid, the second issue for Cartesian methods is how to enforce the correct velocity boundary condition at the interface. The immersed boundary method originated by Peskin [19] is one of the widely used methodologies that introduce a smeared interface; the effect of solid boundaries on the flow velocity is modeled by a set of body forces distributed over the nearby field. A sharp solid wall is instead recovered by the embedded boundary formulation of Yang and Balaras [20], which introduces a field-extension strategy for the velocity and pressure of the computational cells that emerge from solid body motion.

The aforementioned methods and several others are well established for single-phase flow, and their accuracy can be quite high. In developing methods for two-phase flow, an additional layer of complexity emerges because of the numerical treatment of the contact line at the intersection of the liquid-gas interface with the solid boundary: the contact line must be allowed to move, even if such motion is a mathematical paradox because of the no-slip boundary at the solid surface. This situation results in a degradation of the convergence properties of single-phase algorithms for solid body treatment when they are adapted to multi-phase problems.

In the body-conformal finite element method by Baer et al. [21], the slip is imposed at the mesh nodes forming the contact line. In the sharp-interface approach by Liu et al. [22], the level set field in the vicinity of the contact line is redistanced in order to impose a specified contact angle; the slip condition is imposed on grid points in the vicinity of the contact line. In the level-set only method for sharp interfaces and arbitrary boundaries by Krishnan et al. [23], a local, two-dimensional level-set field is reconstructed by fitting the interface to a parabolic curve that intersects the solid surface at exactly the given contact angle. The same embedded boundary approach by Yang and Balaras [20] was later complemented by a level-set based ghost-fluid method to treat gas-liquid interface [24] in the study of wake-ship interaction. In the volume-of-fluid (VOF) continuum surface force (CSF) method by Afkhami and Bussmann [25], the contact line slip is achieved implicitly because the advection scheme for the liquid volume fraction utilizes face-centered velocities; in this way, the center of the cell is removed one half cell width away from the wall. A similar approach is used in this paper, but with the extension of a solid boundary arbitrarily positioned with respect to the Cartesian mesh, whereas in Afkhami and Bussmann (2009) the solid wall coincides with the boundary domain. In fuel injection simulation demonstrations, a level-set based ghost-fluid method for the gas-liquid interface with sharp solid wall treatement was explored by Noël et al. [26] and by Arienti and Sussman [27].

We propose to augment the CLSVOF method with a second level set function to capture the motion of multiple solid boundaries of arbitrary complexity. The level set framework enables contact, merging, and separation of solid boundaries in a more straightforward manner than body surface parametrization or triangulation (used, for instance, by Yang and Stern, 2009). The methodology we propose for the treatment of the contact line is somewhat simpler than the one by Afkhami and Bussmann (2009), but it is demonstrated to be robust for an arbitrary position of the solid wall in two and three dimensions. Finally, there is no need for pressure field extension, as required in the methods by Yang and Stern (2009) and Noël et al. (2012). Given these simplifications, the outcome of the verification tests presented in this paper is rather satisfactory, opening the way to future algorithmic improvements. The validation study with an actual Diesel injector presented later is also relevant, since there appears to be very few studies on the effects of non-trivial orifice geometry on spray formation.

The numerical aspects of the embedded solid boundary algorithm are described first. The method is then verified with a single-phase crossflow passing over a half cylinder at low Reynolds number; the vorticity field arising from the interaction with the curved wall is compared with the results from more specialized, higher-order methods for single-phase flow, showing the lack of computational artifacts and acceptable rate of convergence. Next, the shape of a drop on a wall surface is calculated for different contact angles. The new element in these tests is that the wall is at an angle with respect to the Cartesian axes. The convergence properties of the final drop shape and the rate of volume conservation are discussed, including dynamic cases where the initial drop shape is different than the assigned one.

For validation purposes we consider an early experimental study by Arcoumanis et al. [28], where the flow velocity inside a scaled-up Bosch six-hole transparent Diesel injector was measured with laser Doppler velocimetry for evaluating average and fluctuating components. The asymmetric spray obtained from the simulation is briefly discussed to point out the relevance of an injector simulation that can capture both internal and external flows. The last example concerns a transient injection where the injector’s needle moves relative to its cap. The geometry and motion data belong to a real injector, from the extensive data set by the Engine Combustion Network (ECN) reported in Karstengren et al. [29]; the calculation demonstrates the ease of the proposed methodolgy in dealing with moving boundaries and a changing topology (merging and separation) of the solid boundaries.

2.3 Numerical Method

The Navier-Stokes equations for incompressible flow of two immiscible fluids are solved with the one-fluid approach according to the level-set equations for multiphase flow [30]:

$$\rho(\phi)\frac{D\mathbf{u}}{Dt} = -\nabla p + 2\nabla(\mu(\phi)\mathbf{D}) - \sigma\kappa\ \nabla H(\phi) \tag{1}$$

$$\nabla\cdot\mathbf{u} = 0 \tag{2}$$

$$H(\phi) = \begin{cases} 1 & \phi \geq 0 \\ 0 & \phi < 0 \end{cases} \tag{3}$$

$$\rho(\phi) = \rho_L H(\phi) + \rho_G (1 - H(\phi)) \tag{4}$$

$$\mu(\phi) = \mu_L H(\phi) + \mu_G (1 - H(\phi)) \tag{5}$$

$$\frac{D\phi}{Dt} = 0\,. \tag{6}$$

In the equations, **u** is the vector field, *p* the pressure, ϕ the level-set function, κ the interface curvature, and **D** the deformation tensor, $\mathbf{D} = (\nabla\mathbf{u}+(\nabla\mathbf{u})^{T})/2$; *H* is the Heaviside function and *D*/*Dt* the material derivative; σ is the surface tension coefficient. The smooth zero level of ϕ represents the time-evolving gas-liquid interface. The properties of density, ρ, and dynamic viscosity, μ, are function of ϕ everywhere in the computational domain. The same constant temperature is used for the liquid and the gas phases.

In the coupled level-set/volume-of-fluid (CLSVOF) method, the advection equation for the liquid volume fraction,

$$\frac{DF}{Dt} = 0 \tag{7}$$

is solved in step with ϕ so that the level-set can be re-initialized in a local mass-preserving fix; the liquid volume fraction *F* is used with the interface normal from ϕ to construct a volume-preserving distance function.

The non-linear advection terms in Equation (1) are calculated in non-conservative, semi-Lagrangian unsplit form. Variables are located according to the staggered MAC grid arrangement; see Figure 1. A second velocity field for the liquid phase is extrapolated to the gas phase to advect the VOF function [31]. The liquid velocity is numerically divergence-free in the liquid region (but not necessarily divergence-free in the gas region, which might cause small over- or under-shoots in the VOF function). A full account of the CLSVOF interface capturing method and of the multiphase flow solver developed by Sussman can be found elsewhere (Sussman et al. 2007), together with verification studies of surface tension-driven oscillations of a spherical drop and of ligament pinch-off induced by capillary instability.

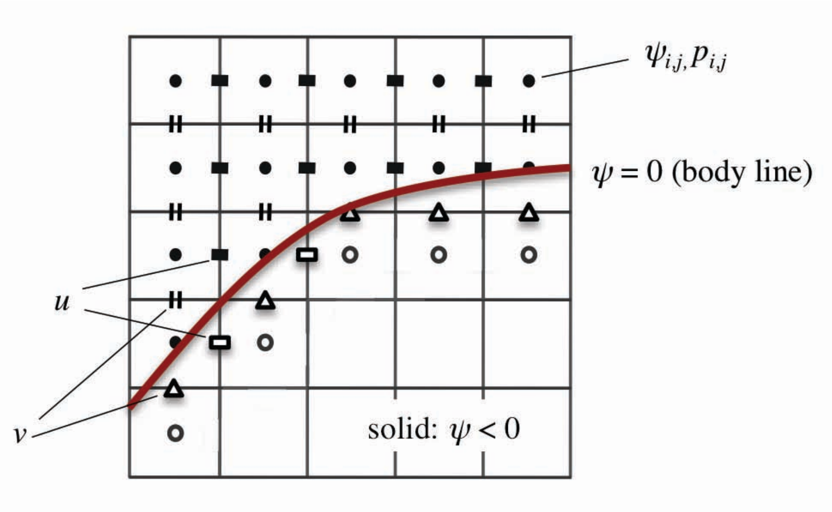

Figure 1. Schematics for face velocity treatment near a solid wall for the MAC arrangement on a Cartesian grid.

2.3.1 Solid wall level set

The solid boundary is represented as the zero level set of a second signed distance function, ψ. By convention, the field ψ is positive outside the body and negative inside it. The magnitude of ψ is the minimal distance between the cell centroid and the surface of the body. This function is calculated using the solid boundary description, which may consist of a parameterized curve or of a triangulation listing the surface nodes and their connectivities. In the latter, more general case, the calculation sweeps over all the triangles comprising the body surface and must account for the possibility that the minimal distance occurs either at the corners of triangle, along the edges of triangle, or inside the triangle.

The methodology described next works for the solid geometries considered in this paper, but the reader interested in a more efficient approach is referred to the report by Mauch in 2000 [32]. Here, for simplicity of implementation and to increase execution speed, the ψ calculation is carried out on an auxiliary Cartesian box, labeled S, which is sized to contain the entire solid body. The result is the auxiliary $\psi_{I,J,K}$; indices in capital letters are used to distinguish the function defined on the auxiliary grid from the local $\psi_{i,j,k}$ function defined on a grid block. The procedure to find the signed distance function from the Lagrangian elements, expressed as a list of elements and node coordinates, is as follows:

1. For elements containing more than 3 nodes, break up the element into multiple triangles (so that each element has exactly 3 nodes).
2. Traverse all elements: for a given triangle, if one of its sides exceeds the mesh spacing of the auxiliary grid, Δx_S, then split the largest side of that element in half in order to form two new triangles. Repeat until no more triangles exist with sides larger than Δx_S.
3. Initialize the signed distance function from the refined element/node list, ψ, to a large positive value. Also, initialize their tag to zero for all the cells.

4. Calculate the node normal $\mathbf{n}_{node}$ as the average of the normals $\mathbf{n}_{element}$ of the adjoining triangles to the node. When required, derive the edge normal $\mathbf{n}_{edge}$ from linear interpolation of the node normals from the two nodes that make up the edge.
5. Traverse all the refined Lagrangian elements:
    a. For each triangle, find the Cartesian cell (I, J, K) whose center is closest to the triangle's centroid.
    b. Traverse the 3×3×3 stencil about cell (I, J, K). For each cell (I', J', K'), check if the projection from its center onto the plane of the triangle is in its interior:
        i. If "yes", compute $d = (\mathbf{x}_{I', J', K'} - \mathbf{x}_{centroid}) \cdot \mathbf{n}_{element}$.
        If tag = 0 or $| d | < | \psi_{I', J', K'} |$ then set $\psi_{I', J', K'} = d$ and tag = 1;
        ii. If "no", then check if the projection is in the interior of the triangle's edge for each of the three edges. If "yes", find the distance from the cell center to its projection on the edge, $d_{project}$. If tag = 0 or $| d_{project} | < | \psi_{I', J', K'} |$ then set $\psi_{I', J', K'} = d_{project} \cdot \mathrm{sign}((\mathbf{x}_{I', J', K'} - \mathbf{x}_{projection}) \cdot \mathbf{n}_{edge})$ and tag = 1;
        iii. If "no", then the closest distance from the cell center to the element must be at one of the element's three nodes. For each node compute the distance d_{node}. If tag = 0 or $| d_{node} | < | \psi_{I', J', K'} |$ then set $\psi_{I', J', K'} = d_{node} \cdot \mathrm{sign}((\mathbf{x}_{I', J', K'} - \mathbf{x}_{node}) \cdot \mathbf{n}_{node})$ and tag = 1.
6. Extend the distance the signed distance function from the cells that have tag = 1 into the cells that are not tagged.

When N solid bodies exist, the corresponding level set functions are generated in sequence, one per body: ψ^1 and $\psi^2, ..., \psi^N$. The functions are then combined on S according to the relation

$$\psi = \min(\psi^1,\ \psi^2, \ldots,\ \psi^N) \tag{8}$$

The reason why the minimum is sought in this operation is the convention that $\psi > 0$ in the fluid region. Evaluating Eqn. (8) cell by cell makes it particularly easy to merge solid bodies without issues of connectivity or of skewed computational cells.

The last step is to quadratically interpolate the auxiliary $\psi_{I,J,K}$ onto the local $\psi_{i,j,k}$ of an AMR block. In case of moving wall boundaries, $\psi_{I,J,K}$ needs to be calculated at every timestep; for stationary solid bodies, $\psi_{I,J,K}$ is only calculated at the beginning of the simulation, whereas $\psi_{i,j,k}$ is interpolated at run-time as requested by the AMR remeshing. The timing of this algorithm is discussed for two cases of fixed and moving boundaries in Sections 4 and 5, respectively.

2.3.2 Boundary conditions at the wall

The components of flow velocity at the wall are made consistent with the no-slip boundary condition through the Poisson equation and the projection operator. The solid wall velocity is first stored for all the nodes in the tessellation. Then, for each cell of the auxiliary grid whose center $\mathbf{x}_{I,J,K}$ is the closest to an element of the tessellation, the value $\mathbf{v}_{I,J,K}$ is assigned as a weighted average of the nodes' values belonging to the element; the weights are defined as the normalized inverse distance of $\mathbf{x}_{I,J,K}$ to the nodes positions. At this point, $\mathbf{v}_{I,J,K}$ is only known in a few cells of S. The values of $\mathbf{v}_{I,J,K}$ are extended in a narrow band from the solid surface by a simple front-advancing procedure where an unmarked cell takes its value from the neighboring cells that have already been marked. The procedure is concluded by the quadratic interpolation the auxiliary variable $\mathbf{v}_{I,J,K}$ onto the local $\mathbf{v}_{i,j,k}$.

In transferring data to the solver's face velocities, it is convenient to refer to Figure 1, which provides a two-dimensional schematics of the conventional MAC grid: cell and face values that need to be populated at every iteration are indicated by empty symbols. For a cell in the fluid region, $\psi_{i,j,k} > 0$, a solid face is a face in which the solid level set function is negative in at least one of the adjoining cell centers: for instance, $\psi_{i,j,k} \cdot \psi_{i+1,j,k} < 0$. The velocity at the $i+1/2$ face is then calculated as the average of the cell values $\mathbf{v}_{i,j,k}$ and $\mathbf{v}_{i+1,j,k}$.

The boundary condition for the pressure projection step can be formally written as

$$\nabla p \cdot \mathbf{n}_{face} = \rho_{i+1/2,j,k}\left(\mathbf{u}^{*}_{i+1/2,j,k} - \mathbf{v}_{i+1/2,j,k}\right) \cdot \mathbf{n}_{face} = 0\,, \tag{9}$$

where $\mathbf{u}^*$ is the provisional field computed from the velocity and volume fraction fields of the previous time step. Thus, in the actual implementation, the Poisson equation is solved under the conditions that $\mathbf{u}^* = \mathbf{v}$ and $\nabla p \cdot \mathbf{n}_{face} = 0$ at solid faces.

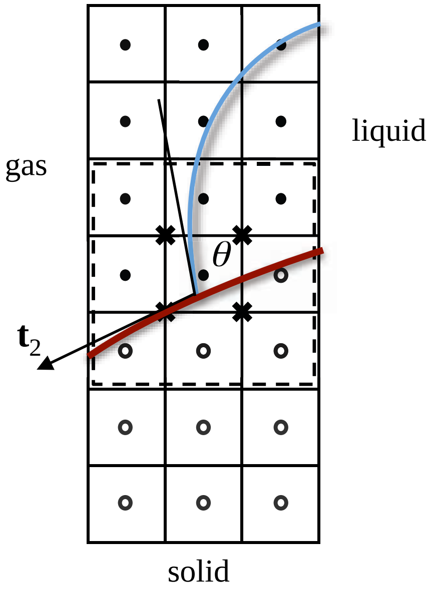

Figure 2. Contact angle schematics. The zero ψ iso-contour (thick red line) represents the solid wall and the zero ϕ iso-contour (thinner blue curved line) represents the gas-liquid interface.

2.3.3 Curvature and contact angle

In calculating curvature at the gas-liquid interface, the “method of heights” based on the level set function ϕ is followed. This procedure can be described for simplicity in two dimensions (see Figure 1 and Figure 2), but it is implemented in the code also for three dimensions. The use of the level set function in the method of heights was introduced in Sussman and Ohta (2009) in a departure from the previous approach in the CLSVOF method (in Sussman et al. 2007 and Stewart et al. 2008) based on volume fraction. It was suggested by Sussman and Ohta (2009) that computing the curvature from the level set function is easier in the context of an adaptive hierarchy of grids and slightly more accurate, especially when two interfaces come in close proximity to each other.

As in the case with the volume fraction, a 5-point stencil needs to be considered for cell (i, j). Curvature is computed if

$$\phi_{i,j} \cdot \phi_{i',j'} \le 0 \quad \text{and} \quad \left|\phi_{i,j}\right| \le \left|\phi_{i',j'}\right|, \tag{10}$$

where (i', j') belongs to the stencil. The only difference with respect to the volume-fraction based method is that to determine the heights h_{i-1}, h_i, and h_{i+1} it is necessary to look at where the sign of ϕ changes, e.g., to find h_i one has to consider the values ϕ_{i,j^*} with $j^* = j-3, \ldots, j+3$.

To implement the contact between the gas-liquid interface and the solid wall, the algorithm for curvature reverts to calculating the divergence of the interface normals,

$$\kappa = \nabla \cdot \mathbf{n}_\phi = \nabla \cdot \left(\nabla\phi / |\nabla\phi| \right), \tag{11}$$

if any cell of the height function stencil is in the solid domain, $\psi_{i',j'} < 0$. The finite difference formulation, albeit less accurate than the method of heights, enables the straightforward enforcing of a prescribed contact angle θ.

The 3×3 stencil necessary for this calculation is represented in Figure 2 by the dashed line. Finite differences between adjacent centers are used to calculate the normal vectors $\mathbf{n}_\phi$ at the corners, identified by crosses in the schematics. If one of the cell centers falls in the solid region, $\mathbf{n}_\phi$ is replaced by the normal determined from θ and from the normal to the local zero solid level set, $\mathbf{n}_\psi = \nabla\psi/|\nabla\psi|$. For this, auxiliary vectors $\mathbf{t}_1$ and $\mathbf{t}_2$ need to be calculated,

$$\mathbf{t}_1 = \mathbf{n}_\psi \times \mathbf{n}_\phi \tag{12}$$

and

$$\mathbf{t}_2 = \mathbf{n}_\psi \times \mathbf{t}_1 . \tag{13}$$

The vector $\mathbf{t}_2$ is tangential to the solid surface and points away from the liquid phase by construction. The contact normal is calculated as

$$\tilde{\mathbf{n}}_{cont} = \mathrm{sign}(\mathbf{n}_{\phi} \cdot \mathbf{t}_2)\ \sin\theta\ \frac{\mathbf{t}_2}{|\mathbf{t}_2|} - \cos\theta\, \mathbf{n}_{\psi} \tag{14}$$

with

$$\mathbf{n}_{cont} = \tilde{\mathbf{n}}_{cont} \big/ |\tilde{\mathbf{n}}_{cont}|. \tag{15}$$

The process is concluded by evaluating the curvature at the face centroids. Surface tension is only applied where *i*) ϕ changes sign across adjoining cells and *ii*) ψ is positive. Because cell face velocities are used, the slip length is always $\Delta x/2$.

2.3.4 Adaptive mesh refinement

Another component of the simulation capability presented in this paper is the use of block-structured, adaptive mesh refinement (AMR) for computationally intensive calculations. Starting from the base level, boxes (with a minimum size of, say, 32^3 cells) are combined to cover all the tagged cells within the assigned coverage efficiency. This new set of blocks with the same grid spacing forms level 1. The refinement ratio between two consecutive levels is two. The new level can in turn be tagged for refinement, and the process is repeated until the input grid resolution is achieved. Data on the fine level are either copied from a previous time step or, when the grid structure has changed locally, they are conservatively interpolated from the underlying coarse level. The liquid-gas interface is always embedded in the finest grid level to avoid gross interpolation errors (Kadiouglu and Sussman 2008).

The definitions and operators necessary to carry out the AMR tasks are provided by the BOXLIB library [33], which is developed and maintained by the Center for Computational Sciences and Engineering group at Lawrence Berkeley National Laboratories.

The advective terms are calculated on all levels, and the updated data on a fine level are averaged down to the underlying coarser one. The sparse matrix system that results from discretizing the pressure correction equation with discontinuous coefficients on the AMR blocks is solved by the multigrid preconditioned conjugate gradient method (MGPCG). Compared to our previous studies on the topic of spray atomization (Li et al. 2010 and Arienti et al. 2013), the current work takes advantage of a new MGPCG method by Duffy et al. [34], which is specifically developed for the adaptive hierarchy of grids. With an optimal blocking factor, it is found that the new MGPCG AMR method no longer consumes the majority of CPU time per timestep as the number of adaptive levels increases.

2.4 Verification tests

2.4.1 Crossflow over a half cylinder

A verification problem for which there is a large pool of numerical and experimental results is the calculation of the two-dimensional flow around a circular cylinder of diameter D. The purpose of this test is to show that the embedded solid boundary technique does not generate artifacts and that the convergence is at least first-order. Flow in the far field is assumed to be uniform, $u = U_\infty$ for $t > 0$. The Reynolds number is defined as $\mathrm{Re} = DU_\infty/\nu$. At sufficiently small values of Re, as in this test, the flow can be considered symmetrical and only a half cylinder is used. The half cylinder is located at $x = 10D$ and side = 0 in a $18D \times 6D$ Cartesian domain with symmetry boundary condition along the bottom side.

Medium and fine grid resolutions are obtained by halving Δx in both coordinate directions, starting from the coarsest grid of 64×192 cells. An even finer grid resolution is calculated with 512×1536 cells.

A close-up of the contours of vorticity around the half-cylinder, both inside and outside the solid boundary, is shown in Figure 3 at Re = 20. The zero iso-contour of the solid level-set corresponds to the red line. No spurious effects due to the embedded boundary implementation are observable, and the plot qualitatively agrees with the one obtained by Calhoun (2002) based on solving the streamwise vorticity equations. The dotted, dashed and continuous lines correspond to the coarse (64/6 cells per unity length), intermediate (128/6) and fine grid resolution (256/6). The finest grid resolution (512/6) coincides almost exactly with the fine grid resolution and it is not shown in the plot.

The convergence properties for this case are listed on Table 1. Since there is no closed-form solution for this flow, we evaluate convergence by comparing two simulations at consecutive grid refinements. The norms are $l_2 = \left(\sum_{i=1}^{N} \delta_i^2\right)^{1/2}$, $l_1 = \sum_{i=1}^{N} |\delta_i|$ and $l_\infty = \max_N |\delta_i|$, where $\delta = \{\delta_i\}$ is the vector difference of the field values (the two components of velocity and vorticity) taken from two consecutive grid resolutions; N is the total number of grid points of the coarser of the two grids. Thus, the column in Table 1 that is labeled “fine-xfine” lists the norms of the difference vector between the 256×768 grid and the 512×1536 grid, with one grid point every two skipped on the latter. Finally, the last column in Table 1 is the convergence rate calculated from the slope of the linear fit of the three points listed on each row. Note that the l_1 and l_2 norms are divided by N. The l_∞ norm shows most clearly that the convergence rate is of first-order for the two components of velocity and of zeroth-order for vorticity. The computational cells with the largest difference between two consecutive grid resolutions are located, as expected, at the boundary of the solid body.

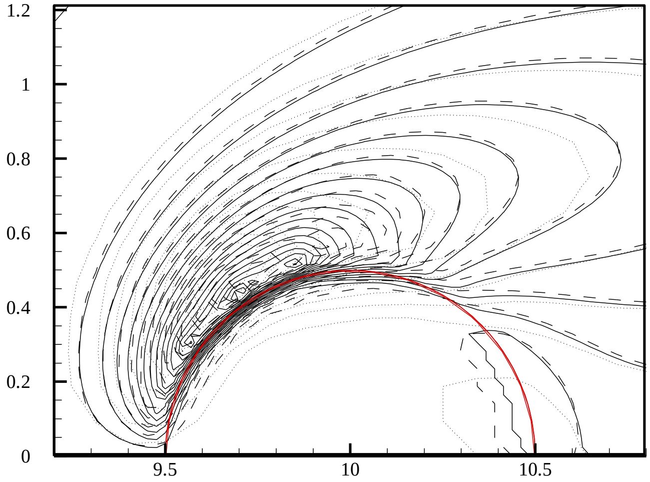

Figure 3. Contours of vorticity around a half-cylinder in crossflow at Re =20. The contours, from -6 to 0 in steps of 0.2, are superimposed to the zero solid level-set line (in red), which represents the boundary of the cylinder. The dotted, dashed and continuous lines correspond to the coarse (64/6 cells per unity length), intermediate (128/6) and fine resolution (256/6).

The last element of this test is the evaluation of the reattachment length L from the cylinder's trailing edge. Values at Re = 20 and Re = 40 are listed on Table 2 as a function of grid spacing. The differences of consecutive values of L are 0.251, -0.086 and 0.018 for Re = 20; and 0.503, -0.214 and 0.039 for Re = 40. These differences correspond, in both cases, to a more than linear convergence. The experimental results of Dennis and Chang [35] and the numerical results of Calhoun [36] are also listed on Table 1: the measured reattachment lengths fall between the results from the present calculations and the values reported by Dennis and Chang (1970).

Table 1. Error norms and convergence rates for the two components of velocity (u_x, u_y) and vorticity ω_z for pairs of increasingly finer grids.

	Coarse-medium	medium-fine	fine-xfine	convergence rate
u_x				
l_2/N	0.0011935	3.2936e-4	2.7023e-5	2.73
l_1/N	0.027651	0.015710	0.0022279	1.82
l_∞	0.14596	0.070753	0.035915	1.01
u_y				
l_2/N	7.5492e-4	8.2722e-5	1.1274e-5	3.03
l_1/N	0.069099	0.0044771	0.0009688	3.08
l_∞	0.14596	0.041539	0.035915	1.15
ω_z				
l_2/N	0.0055727	0.0016805	0.0005150	1.72
l_1/N	0.064975	0.028570	0.0098922	1.36
l_∞	1.81089	2.22074	1.81129	-1.60e-4

Table 2. Reattachment length *L* evaluated from the cylinder's trailing edge as a function of grid spacing.

	$\Delta x/D$ = 0.09375	0.04688	0.02344	0.01172	Dennis & Chang (1970)	Calhoun (2002)
L (Re = 20)	0.825	1.076	0.990	1.008	0.94	0.91
L (Re = 40)	2.130	2.633	2.419	2.458	2.35	2.18

2.4.2 Oscillating cylinder

The cylinder is now subject to the horizontal motion

$$x = -A\sin(2\pi f\ t) \tag{16}$$

The two relevant parameters for this flow are the Keulegan-Carpenter number, KC = $U_{\max}/(f\,D)$ = $2\pi A/D$ and the Reynolds number Re = $U_{\max}D/\nu$. The values used here, KC = 5 and Re = 100, correspond to a regime of periodic, symmetric vortex shedding.

Unphysical, temporal oscillations of the pressure fields have been reported for non boundary-conformal methods when the body is moving or deforming. The primary source of this error is that some computational cells belonging to the solid suddenly become active fluid cells. Seo and Mittal [37] make the case that the violation of local mass conservation near the immersed boundary causes these spurious pressure oscillations.

In Figure 4, the drag coefficient derived from an oscillating cylinder calculation is compared with results from Dütsch et al. [38]. The calculation is started from a quiescent field and integrated in time for 3 cycles, until periodic vortex shedding is established. The computational domain is $16D \times 8D$, with $\Delta x = 0.0156D$ and $\Delta t = 0.008\ D/U_{max}$. The cylinder is located at $x = 8D$ and $y = 0$.

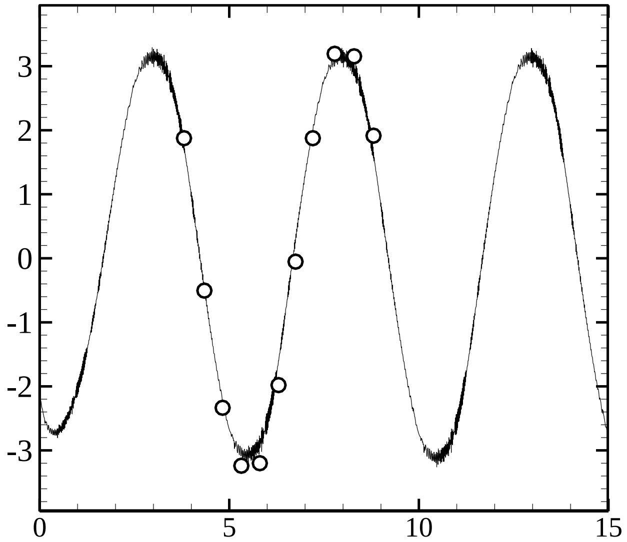

Figure 4. Drag coefficient as a function of time. Comparison with results from Dütcsh et al. 1998.

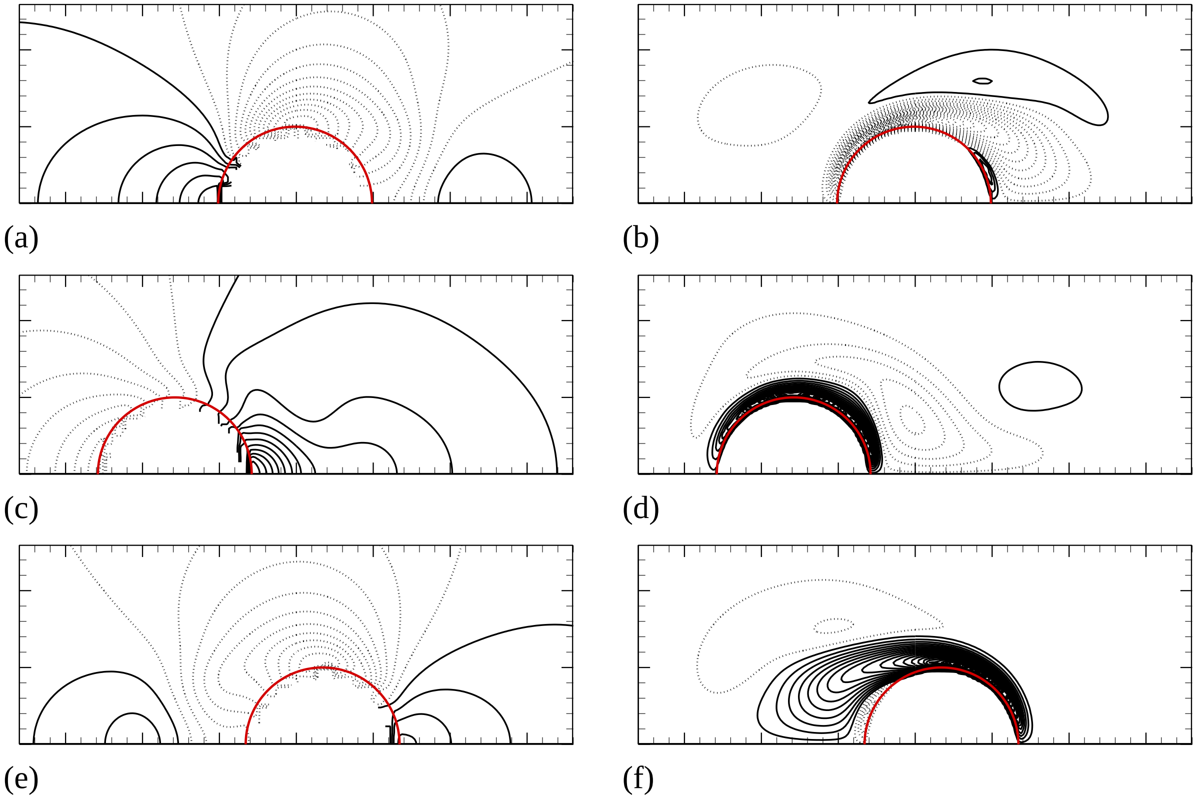

(a)
(b)
(c)
(d)
(e)
(f)

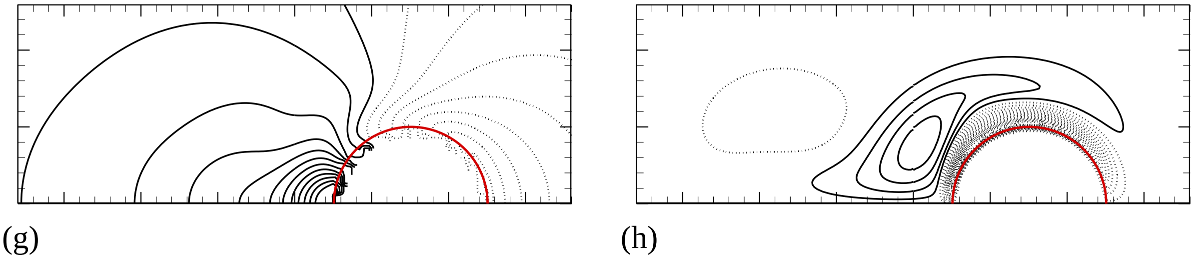
(g)

(h)

Figure 5. In-line oscillating cylinder in a fluid at rest (Re = 100 and KC = 5). Pressure and vorticity contours at four different phase-angles. -1.1 < *P* < 1.1 with intervals of 0.09 and -26 < ω < 26 with intervals of 0.95. (a) 0°; (b) 96°; (c) 192°; (d) 288°. Dashed lines correspond to negative iso-values.

The good agreement with the calculation by Dütsch et al. (1998) is encouraging, considering that their result was obtained with the much more problem-specific configuration of a body-conformal grid oscillating with the cylinder and that the wall grid resolution in the two cases is comparable. The pressure artifact is rather modest for this particular choice of Δx and Δt, even though the drag coefficient exhibits some ringing, visible at the crests and troughs of the curve in Figure 4. In agreement with the error analysis by Seo and Mittal (2011), we indeed observed increasing spurious oscillations if the same simulation was run with a much smaller timestep but with the same grid spacing.

The pressure and vorticity flow fields, as shown in Figure 5, are also devoid of spurious effects. As the cylinder moves to the left, a thin boundary layer develops from the upper wall and eventually detaches in a vortex (the same process would occur symmetrically on the bottom half of the cylinder). Vortex generation stops when the body reaches its extreme left location, as shown in frames (c)-(d). Then the cylinder moves backwards, and the same process takes place on its right side. The flow fields in Figure 5 compare well with the analogous plots in Dütcsh et al. (1998) and Yang and Balaras (2006) and indicate that the present method can properly capture the dynamics of the vorticity field. This and the previous tests suggest a convergence rate that is approximately linear with grid refinement. Such a low order of convergence, compared to already existing methods specialized for single-phase flow, is not a concern as we tackle the interaction of the liquid-gas interface with the solid boundary. In that more challenging context we will show that linear convergence or higher is maintained, at least in the case where the static contact angle is 90°.

2.4.3 Static drop on a horizontal plane

We first consider a half-drop on a plane aligned with one coordinate direction. Simulations are carried out first in two dimensions for ease of discussion. As in all the other tests in this Section, the density of the liquid is 1000 kg/m^3 and the density of the gas is 1.20 kg/m^3. The viscosities of the two phases are 0.0010 kg/m-s and 1.78·10-4 kg/m-s, respectively. Surface tension is 0.0709 N/m. A symmetry plane is established at the left of the domain with outflow boundary conditions at the other sides. The computational domain is a square with 32×32 cells. For contact angle θ =

90^o, the initial condition with symmetric boundary is a quarter of a circle with radius slightly larger than eight computational cells.

In Figure 11, the shape of the drop after 100 iterations (when the solution approximately reaches steady state) can be compared with the exact solution, drawn as a dashed line. It appears that the final shape of the drop depends in part on the location of the solid wall. Two cases are considered: in Figure 6(a), the $\psi = 0$ line overlaps cell faces whereas in Figure 6(b) the line $\psi = 0$ passes through cell centroids. The wall-at-the-cell-face case corresponds to an almost flawless initial reconstruction of the half circle, which is essentially preserved in the rest of the simulation. This is shown by the superposition of $\phi = 0$ isocontours drawn at regular intervals. The maximum variation (in absolute value) of the drop volume with respect to the initial condition is very small: 0.02%.

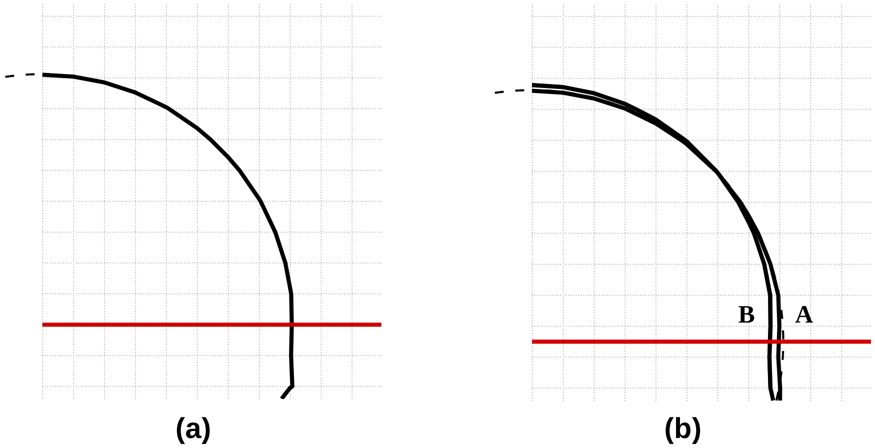

(a) (b)

Figure 6. Effect of wall location for static drop. The starting and prescribed angles are both the 90^o angle. The curved continuous lines are the $\phi = 0$ isocontours at different times. In frame (a), the wall (thick horizontal line) overlaps the cell faces: all the isocontours overlap. In frame (b), the wall passes through the cell centroids. The exact solution is shown as a dashed circle line. Line A is drawn at time *t* = 0; line B is drawn after five time steps.

Conversely, the wall-at-the-cell-centroid case is the least ideal situation: the wall boundary treatment is unable to correctly reconstruct the curved surface, which appears flattened at the contact point. This unbalance triggers a small oscillation ($\sim \Delta x/2$) of the drop shape, which eventually stabilizes in a slightly oblong shape. The maximum variation of the drop volume with respect to the initial condition is larger than in the previous case, but still rather modest for this grid resolution: 0.85%. We verify that the drop shape outcome is intermediate when the solid wall traverses an intermediate position between the centroid and the cell face.

2.4.4 Effect of changing contact angle

A second set of tests consists in starting from the quarter of circle shape and assigning a contact angle different than 90^o. The response of the drop provides an indication of the behavior with a dynamic contact angle. The dependence on the position of the solid wall is examined for $\theta = 120^o$ contact angle (Figure 7) and for $\theta = 60^o$ angle (Figure 8). The notation and the initial conditions are the same as in the previous test. The initial drop radius is $R_0 \cong 8\ \Delta x$.

The steady-state solution is a truncated circle with the same area. The final radius, R_θ (in radians), is a function of the contact angle $0 < \theta < \pi$,

$$R_\theta = \sqrt{\frac{\pi}{2\theta - \sin 2\theta}}\, R_0. \qquad (17)$$

Clearly, $R_\theta\ (\theta = \pi/2) = R_0$. The value of R_θ is used to draw the circular arc corresponding to the exact solution in Figure 7 and 8.

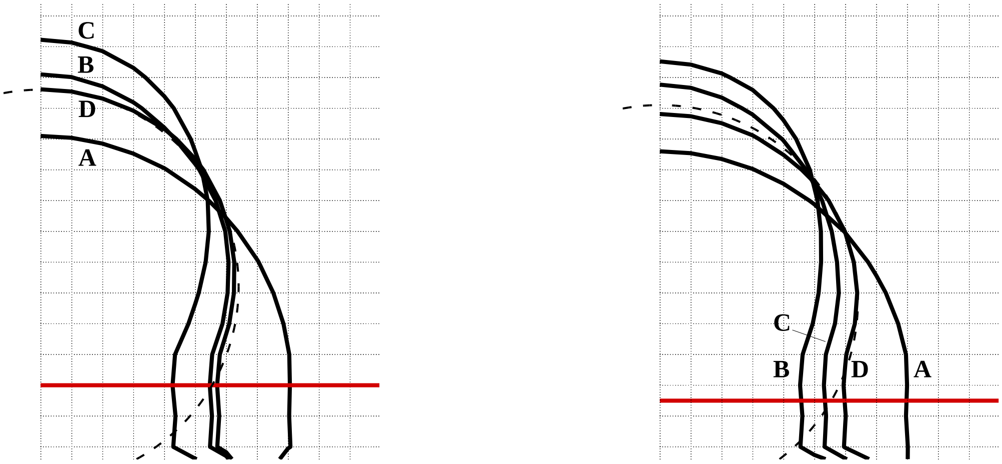

(a) (b)

Figure 7. Effect of wall location for a drop with 120^o contact angle starting at 90^o. The curved continuous lines are the $\phi = 0$ isocontours at different times. In frame (a), the wall (thick horizontal line) overlaps the cell faces. Line A is drawn at time *t* = 0; line B and C after one and two time steps; line D after 15 time steps. In frame (b), the wall passes through the cell centroids. The exact solution is shown as a dashed circle line. Line A is drawn at time *t* = 0; lines B and C after three and five time steps; line D after 15 time steps.

The steady-state solution is reached within a few hundred iterations. In the case of wall at the cell face, the average area variation with respect to the initial value is 0.13% with maximum variation of 0.28%. For the same contact angle, but with the wall located at the cell centroid, the average variation is 4.1%, with maximum variation of 7.7%.

A closer examination of Figure 7(a) indicates that the 120^o angle is not represented exactly. The correct drop shape begins to be recovered in the first cell away from the solid wall, leaving an artifact of size Δx. The size of the artifact increases to 3/2 Δx in Figure 7(b) because the location of the solid wall is just such that the cell containing the contact point is not active ($\psi_{i,j} < 0$). This discrepancy causes the drop to be slightly deformed with a larger area variation compared to the face-aligned case.

A similar behavior is observed for the 60^o contact angle. Figure 8 underscores that the cell containing the contact point cannot resolve the correct contact angle, but that the drop profile away from that cell is captured correctly. As in the previous examples, there is a dependency of the result on the location of the solid wall. Particularly, the average value of area variation with respect to the initial value is 0.11%, with maximum 0.40%, when the wall is located at the cell face. With the wall located at the cell centroid, these variations are larger and similar to the values for the 120^o contact angle case. The case in Figure 8b is arguably the worst in terms of position of the solid wall: by displacing the wall downward by a tiny fraction of the grid size, the cell intersected by the solid wall becomes an active cell, and the simulation (not shown here) recovers area variations as small as the ones in the cell-aligned case.

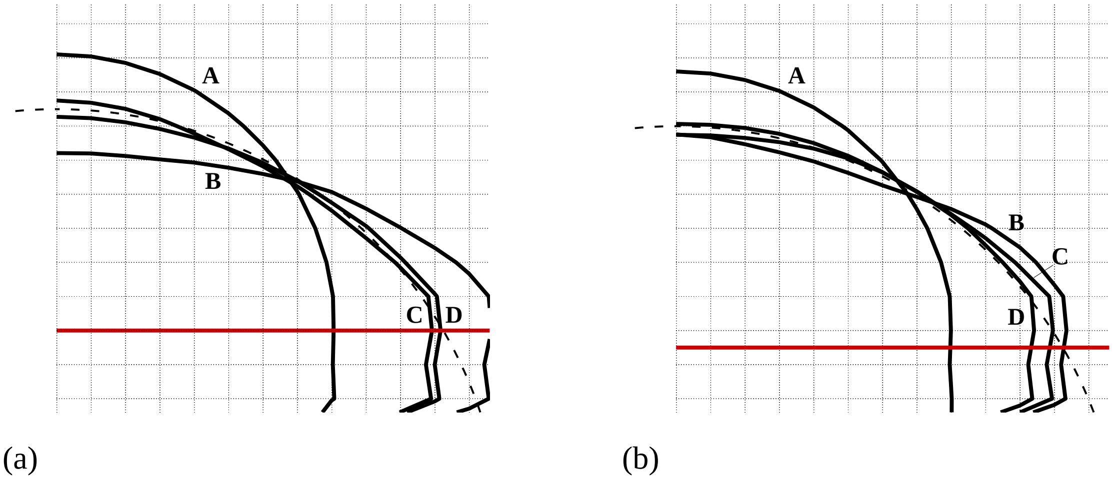

Figure 8. Effect of wall location for a drop with 60^o contact angle starting at 90^o. The curved continuous lines are the ϕ = 0 isocontours at different times. In frame (a), the wall (thick horizontal line) overlaps the cell faces. Line A is drawn at time t = 0; lines B and C are drawn after one and two time steps; line D, after 15 time steps. In frame (b), the wall passes through the cell centroids. The exact solution is shown as a dashed circle line. Line A is drawn at time t = 0; line B and C after one and five time steps; line D after 15 time steps.

2.4.5 Convergence study for a static drop on an inclined plane

A more general situation with respect to the static drop test of Sub-section 2.4.3 is when the wall is not aligned with a Cartesian direction. Since the previous tests indicated artifacts on a size at most comparable with the grid size, we expect to recover linear convergence with grid refinement even in this case. Contact angles of 90°, 120°, and 60° are considered, but this time with the solid wall inclined at an angle of 18°. Starting from a computational grid corresponding to 8 cells across the drop diameter, grid resolution is increased by a factor of two until there are approximately 256 cells across the diameter, as shown on Table 3.

The metrics used for this test are the percentage variation with respect to the exact drop height, e_0 (calculated in the normal direction to the wall),

$$e_0 = \left(1 + \cos(\pi - \theta)\right) R_0, \tag{18}$$

and the percentage variation with respect to the base length, L_0,

$$L_0 = 2 \sin(\pi - \theta) R_0. \tag{19}$$

To evaluate the simulation values of the height and base of the drop, the $\phi = 0$ iso-contour needs to be intersected with $\psi = 0$. This is accomplished by looking at the edges of the zero level of the function $\xi = \min(\phi, \psi)$, which is used in post-processing to exclude the ghost region portion of the drop.

The variations in e and L capture the drop shape deformations, so that a narrower base, for instance, corresponds to a larger height. Area fluctuations due to the treatment of the liquid surface can be completely ignored for 16 or more cells per diameter.

For $\theta = 90°$ the convergence of L to $2R_0$ is more than linear and that the difference with respect to the exact value is quite small. A similar trend is found for the convergence of e to R_0. For instance, for $\Delta x/D = 1/32$, the drop recovers almost exactly the shape of a half circle, narrower at its base (-1.3%) and slightly taller (+0.16%) The small error and super-linear convergence rate are of course due to the 90° contact angle, which forces a condition close to symmetric boundary and benefits from a curvature evaluation almost as accurate as that away from the solid boundary.

For contact angles larger or smaller than 90°, the discrepancy in height and base length increases substantially. For instance, if $\theta = 60°$ and there are only eight computational cells across the drop diameter, the drop shape is sufficiently deformed to suffer rather large deviations in L and e. However, with $\Delta x/D = 1/32$, the error becomes of the order of 1% or less. A similar behaviour is observed for $\theta = 120°$. For both angles, the rate of convergence is linear, or less than linear but never below 0.5. Tests carried out with different plane inclinations confirm the reduction of the convergence order if the contact angle is not ninety degree. A similar outcome is reported by Afkhami and Bussmann (2009) for the contact line curvature of a three-dimensional drop resting on a Cartesian boundary: with their special setting, the curvature converged quadratically for $\theta = 90°$ and linearly for other contact angles.

This test concludes a rather extensive examination of the proposed embedded boundary algorithm. The rate of convergence is on average first order, and, when present, artefacts are only of the size of one grid spacing near the contact point. The examples that follow demonstrate the robustness of the method in two-phase flow simulations. Thus, while simpler with respect to existing, but less general, algorithms (because limited to contact point treatment with specially aligned boundaries, or to single-phase flow), the current staircase approach constitute a good starting point for future improvements.

Table 3. Convergence for a drop at different contact angles on a plane inclined by 18° for three contact angles 90°, 120° and 60°; *e* is the height of the drop at rest and *L* is the base length.

	$\Delta x/D$ = 1/8	1/16	1/32	1/64	1/128	1/256	Convergence Rate
90°							
ΔL (%)	0.08995	-1.804	-1.296	-0.02686	-0.1076	0.02589	1.14
Δe (%)	0.07685	-0.05861	0.1599	0.08282	0.02847	7.879e-4	2.69
120°							
ΔL (%)	8.6273	0.4063	0.5106	0.8001	0.7584	0.2524	0.632
Δe (%)	0.2148	0.8081	0.3105	0.5934	0.07909	0.06727	0.500
60°							
ΔL (%)	-18.99	-5.258	0.01349	1.098	-0.9131	-0.6358	0.735
Δe (%)	-1.971	-1.863	-1.045	-0.5870	-0.1089	0.03595	1.20

2.5 Validation with Diesel injector data

The injector chosen for the validation calculation is the scaled-up Bosch six-hole diesel nozzle by Arcoumanis et al. (1998). The nozzle was manufactured at a 20:1 scale to allow flow measurements inside the sac volume and the injection holes; the nominal hole size of the model was 3.52 mm, which corresponds to about 0.176 mm in the real injector. The conical element (the needle) was placed at 6 mm above its seat, at the maximum lift of the second stage of a two-stage injector. A cross-sectional view of the sac and the cylindrical orifice tube is shown on Figure 9.

The test fluid had density and kinematic viscosity of 893 kg/m^3 and $1.64\cdot10^{-6}$ m^2/s, respectively. The measured flow rate of the 6 mm lift configuration was $5.8\cdot10^{-4}$ m^3/s, corresponding to the average velocity of 10.2 m/s reported by the authors for the orifice. Based on this velocity and on the orifice diameter, the Reynolds number is approximately $2\cdot10^4$. LDV measurements were taken in vertical planes across the injection hole; as shown in Figure 9, the planes were located at 9.5, 10.5, 13.5 and 16.5 mm from the axis of symmetry of the injector.

The measured pressure difference across the transparent injector was 0.85 bars, giving a total discharge coefficient of the needle seat and injection holes of 0.78. Because the pressure in the recirculation zone at the entrance to the hole could decrease below the vapour pressure of the liquid, the occurrence of cavitation could not be excluded in the experiment. The onset of cavitation was found to strongly depend in the experiment on the needle lift and eccentricity, but cavitation is actually not modelled in the simulation presented here.

The surface tension coefficient used in the simulation is 0.024 N/m. The static contact angle is 90°. An important difference with respect to the experimental setup is the absence of the expansion tube that collects the test liquid after passing the orifice: in the problem setup the liquid is injected into air at standard conditions. This setting may affect the exit velocity of the jet, but has the advantage of showing the direct link between spray characteristics and nozzle internal flow.

For ease of discussion, we will refer to the side where the sac is located as “bottom”, in the negative y direction of Figure 9. The uniform inlet boundary velocity is applied along the open area that is visible at the top side in the figure to deliver a sixth of the mass flow rate reported in the experiment. However, to reduce the computational cost, the simulation includes only a quarter of the injector and one of the six orifices. This configuration is displayed in Figure 10. The domain of 100×100×40 mm is sufficiently large to include the development of the jet for several orifice diameters downstream of the orifice exit. With a coarse mesh of 80×80×32, the four levels of adaptive refinement used in the simulation provided the finest grid resolution of 0.0781 mm in the liquid phase. The orifice diameter measures approximately 45 grid cells.

The injector walls were described by a triangular mesh of 28,800 elements with smallest grid size of 0.4 mm. Within one solution cycle, the handling of the solid wall required 5.7% of the CPU time, much less than the treatment of the gas-liquid level set (34.7%), the pressure solve iterations (33.4%), and the nonlinear advection term solution (15.5%). This cost does not include the calculation of the solid level set, which is performed only once on the auxiliary grid at the start of the simulation. In the interval used for this analysis, the average sum of all the computational cells was $3.7 \cdot 10^7$. Calculations were carried out on the Redsky Sandia cluster using (on average) 48 SUN X6275 blades (2.93 GHz dual socket/quad core configuration with 12 GB RAM per compute node).

Upstream of the injection hole, a time-averaged pressure drop of approximately 0.75 bar occurs through the portion of the injector that is included in the calculation. This value compares well with the value 0.78 reported in the experiment. The highest flow velocities in the internal flow occur at the upper corner of the hole inlet, where the lowest fluid pressures can be expected. This is clearly visible in Figure 9, where the Reynolds-Averaged Navier-Stokes (RANS) velocity field reported in Arcoumanis et al. (1998) (Figure 9a) is compared with a snapshot from the current simulation (Figure 9b). In the RANS calculation, turbulence was simulated by the two equation k-ε model on a coarser, co-located, non-uniform, non-orthogonal numerical grid. In the snapshot from the CLSVOF simulation, only one in twenty vectors is shown, due to the much greater grid density than in the RANS calculation; the continuum black line is the intersection of the $\psi = 0$ iso-contour with the slicing plane.

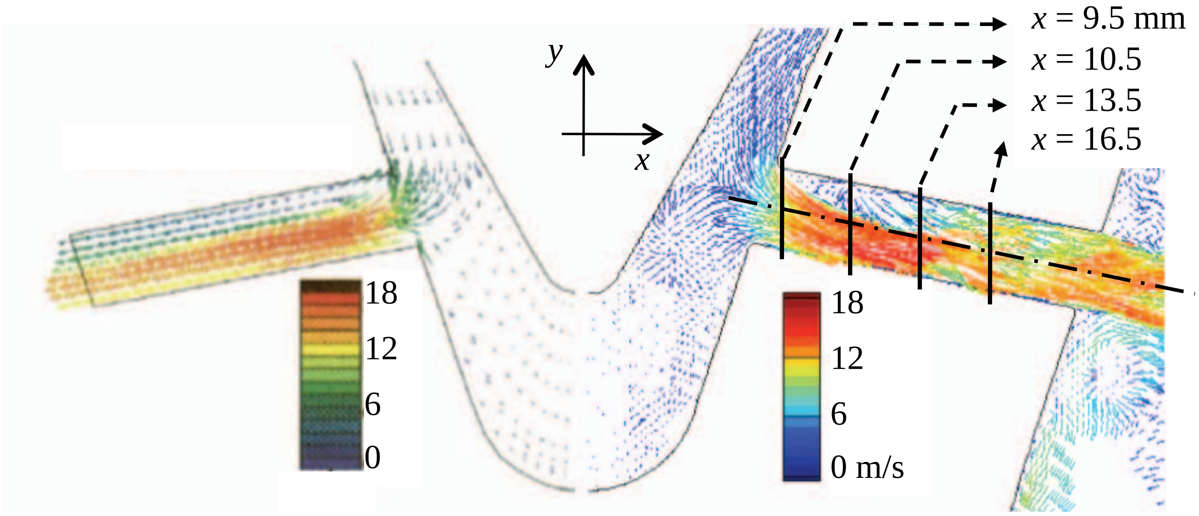

(a) (b)

Figure 9. Vector flow field along a domain cross-section. A RANS simulation result from Arcoumanis et al. (1998) in frame (a) compared to an instantaneous snapshot from the present calculation in frame (b).

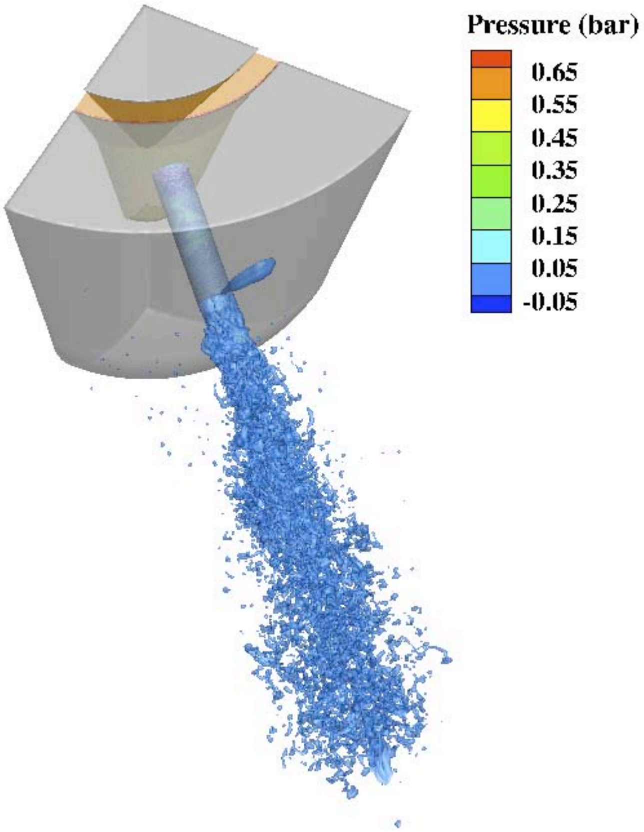

Figure 10. Terminal tip of the injector. Simulation snapshot at time t = 35 ms of the full domain.

The examination of several snapshots suggests that the recirculation re-attaches approximately past half of the hole. For a more quantitative analysis of the flow, the mean and root mean square (rms) velocity are compared to the LDV measurements in Figure 11. The plots are drawn along the orifice radius from the four cross-sections shown on Figure 9b and normalized by the mean orifice velocity of 10.2 m/s. In each plot, the distance of the axial coordinate is counted from the top of the cross-section and normalized by the diameter of the cross-section.

The velocity mean values compare favorably with the experiment; however, the measured recirculation zone is broader and longer than in the simulation and faster acceleration of the computed flow can be seen at x = 13.5 mm. Where data points exist near the walls, it can be noted that are the computed boundary layer is thicker: this aspect can be attributed lack of resolution near the wall, or to the absence of a turbulence model near the wall. For this Re = 10,000 case, we find that the average wall shear velocity, $u_{\tau} = (\tau_w/\rho)^{1/2}$ is of the order of 0.02 m/s, corresponding to a location in wall units of the first point away from the wall of $r^+ = \Delta x\, u_\tau / \nu \sim 1$.

Pressure fluctuations with respect to the average cross-section value (not shown here) are mostly positive in the upper half of the exit orifice, consistently with the lower mean velocity values in that zone. Occasionally, negative pressure variations are observed in the upper half because of flow unsteadiness. The measured rms values of velocity are however consistently larger than in the calculation, with the largest discrepancy in the recirculation zone (this rms peak is similarly lost in the RANS calculation from Arcoumanis et al. 1998). Velocity fluctuations near the orifice's walls are actually of the correct magnitude, but they decrease toward the center of the orifice. This defect in rms is common to under-resolved simulations that attempt to capture the unsteadiness of turbulent flow without a turbulence model. It is also possible that cavitation near the entrance of the orifice contributes to the large fluctuations there. A cavitation model will need to be added in future validation studies.

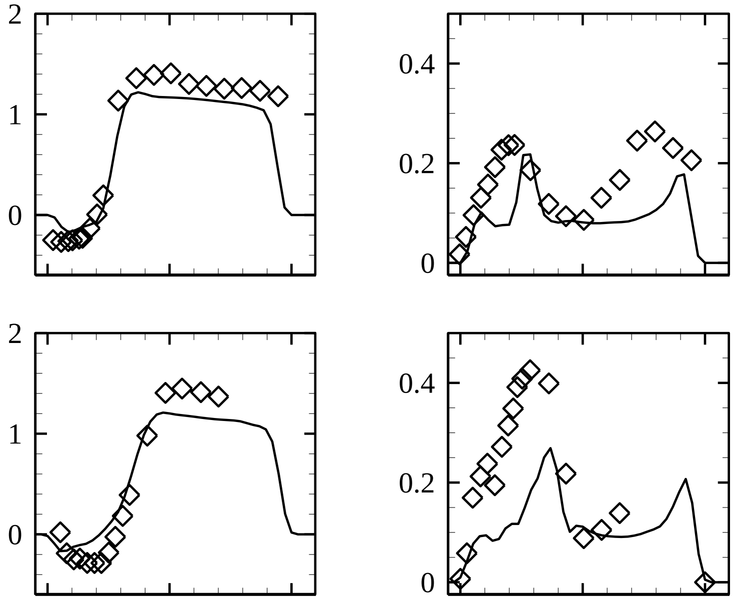

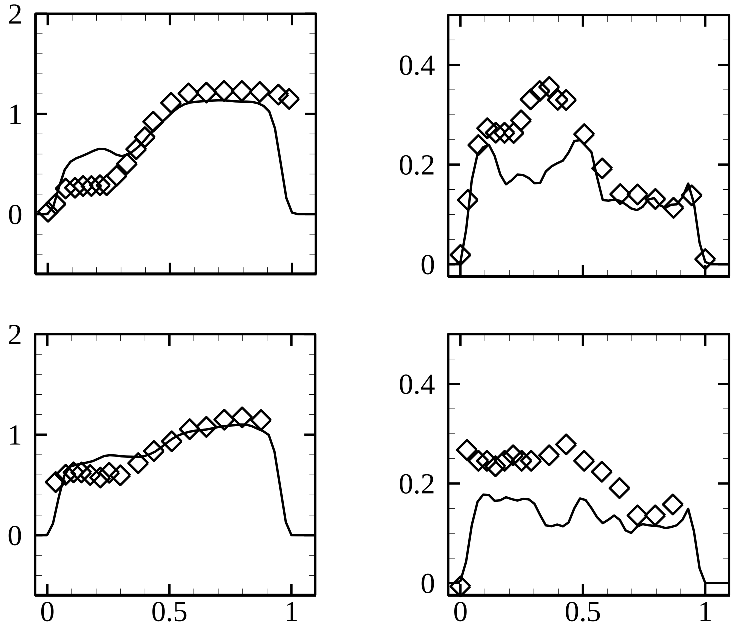

Figure 11. Comparison with LDV measurements along the injection hole. The symbols correspond to measurements, the line to calculated results. Left column: mean axial velocity along the injection orifice at four cross-sections along the injection hole (see Figure 9 for reference). Right column: root mean square values of axial velocity. From top to bottom: *x* = 9.5, 10.5, 13.5, and 16.5 mm.

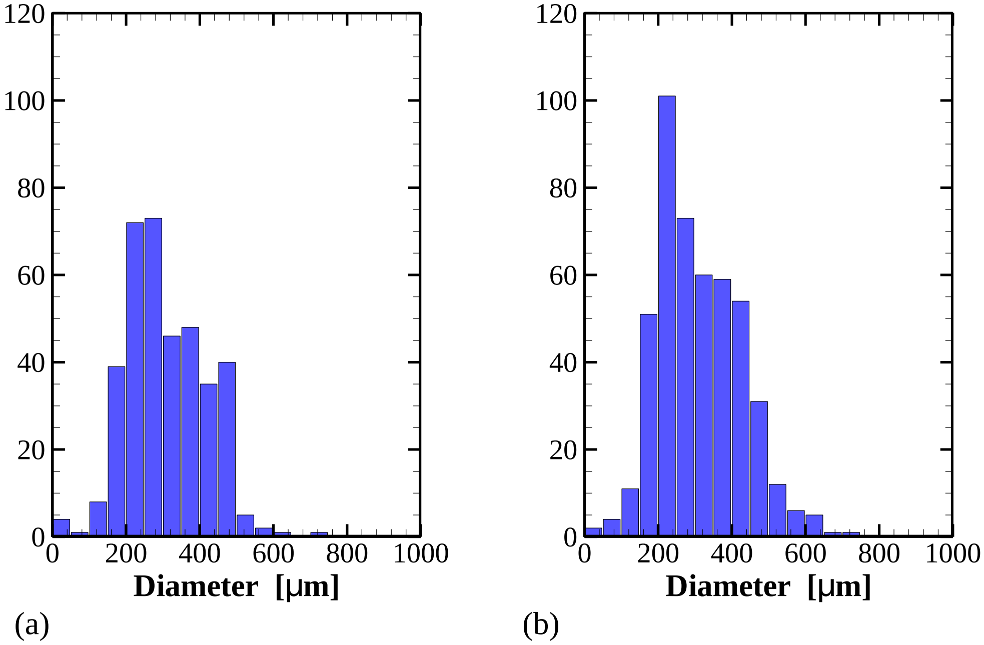

Figure 12. Droplet size distribution in the half the spray that is closer to the injector's tip (a) and farther away (b) at *t* = 35 ms.

Considering now the process of spray formation, in Figure 10 a few drops larger than the orifice diameter can be observed in the initial build-up of the jet, with one large drop attached the injector’s wall. Droplets begin to detach from the jet approximately two orifice diameters downstream of the hole, and from there a complex network of ligaments and drops rapidly consumes the liquid core.

The most apparent feature of the jet outside the nozzle is that it slightly bends upward (in the positive y direction in Figure 9), away from the tip of the injector. This is due to the occurrence of larger velocities in the bottom half of the orifice compared to the upper half. As the faster side of the jet spreads less outwardly, it is relevant to interrogate the simulation about the corresponding drop size. Droplets are identified as isolated blobs from the $\varphi = 0$ liquid surface. Their volume is translated into the effective diameter of the same-volume sphere, producing a histogram of diameter distribution. The one shown in Figure 12, for a snapshot taken at $t = 35$ ms, seems to suggest that the half of the spray that is closest to the tip of the injector has fewer droplets in the range from 200 to 400 mm. At this point, as with the other results reported in this section, more data would need to be collected before quantitative statements can be made

2.6 Demonstration with moving parts

The last test consists of an instance of rigidly moving wall that is used to demonstrate the flexibility of the new method. The test takes advantage of current efforts by the Engine Combustion Network (ECN) to characterize the internal geometry of automotive injectors. Five nominally identical Diesel Bosch injectors with single axial orifice form the baseline that is presently identified as “Spray A” (ECN 2012). X-ray tomography, X-ray phase-contrast imaging, silicone molding, and optical microscopy are combined in this effort to define a database of the internal geometry (including deviations from the nominal shape) in a format that is immediately accessible to simulation. The ECN makes also available a trajectory file with the three-dimensional motion of the needle determined from X-ray phase-contrast and recorded by a high-speed camera.

Three snapshots of the needle motion are displayed in Figure 13. The needle tip (in green) translates according to the specified trajectory with respect to the injector cap. For instance, in its fully open position in frame (a) the base of the needle is outside of the computational domain, to the left of the dashed line: the lift of the needle from its seat opens an annular passage to the liquid. Conversely, in frame (b) the needle base is almost completely inside the computational domain. Frame (c) shows the measured deviation of the needle motion from a perfectly axial trajectory and the resulting non-axisymmetric annular passage. As in all the other injectors of the Spray A batch, the SN 210675 geometry [39] used in this test is affected by slight manufacturing defects: off-center position with respect to the sac, tapering of the hole, and deviation of its cross-section from a perfectly circular shape of diameter 90 mm. These geometrical characteristics are discussed by Kastengren et al. [29].

In the CLSVOF simulation, the solid velocity necessary to populate the boundary condition of the needle is calculated directly by differentiation of the displacement values in the trajectory file. The measured injection pressure of 155 MPa is applied as constant boundary value at the boundary face. The exit pressure is applied to the other five sides of the computational domain box. The gas phase has density of 22.8 kg/m^3, corresponding to an ambient pressure of 6 MPa at

900 K; the liquid gas/density ratio is therefore 30.8. The dynamic viscosity of the liquid is 0.00613 g/cm-s; the dynamic viscosity of the gas is 0.00022 g/cm-s. The surface tension coefficient used in the simulation is 0.024 N/m. The static contact angle is 90°.

The base computational domain is a Cartesian 64×64×192 box with the longest side oriented along the injector's axis measuring 5.1 mm. Two levels of refinement are added to obtain the minimum grid spacing of 6.64 mm. The resulting 13.5 cells per orifice diameter, while adequate for this simple demonstration, are obviously not sufficient for an in-depth study of Diesel injection during transients.

The average sum of all the computational cells was $1.0\ 10^7$ in the interval used for this study. Timing the simulation shows that the handling of the solid wall rises to 47.3% of the CPU time within one solution cycle, and it is now comparable to the pressure solve iteration (45.4%). The third most expensive item is the solution of the nonlinear advection term (4.4%). The increased CPU time percentage is due to the calculation at every time step of the needle level set ψ_2, which is carried out on an auxiliary grid of 93×93×144. It is noted, however, that the full calculation of ψ_2 is not strictly necessary in this case because of the simple motion of the solid body, and that a faster algorithm for this task could be easily implemented even for a more complex trajectory.

The representation of the injector's moving geometry and the pressure boundary condition enable a realistic variation in time of mass flux through the orifice. To illustrate this point, Figure 14 shows the pressure field on a section plane passing through the axis of the injector in a close-up of the full computational domain. The black line corresponds to the intersection with the instantaneous jet surface; the red line is the intersection with the solid wall. Contours of pressure inside the solid domain are due to the overlapping of refinement levels (therefore their variation in time bears no physical significance).

The first frame in Figure 14 captures a moment before the needle returns to its seat, when pressure in the liquid phase gradually decreases between inlet and orifice exit. The second frame displays the partial closure of the flow in the upper half (negative y direction in the plot reference) of the injector. The flow upstream of the contact line finds its way only through the bottom passage, therefore the pressure drop is more localized near the constriction. The jet outside of the orifice still maintains a turbulent appearance, with drops forming a few diameters downstream.

In the third frame of Figure 14 the passage between needle and cap has closed, the mass flux through the pressure inlet has dropped to zero, and the pressure in the sac and orifice region is at this moment slightly lower than in the outside environment. The jet carries a residual momentum, but its appearance has reverted to laminar and drop formation is much delayed. A large chunk of liquid is on the point of detaching from the remaining liquid in the sac. Sequences of the three-dimensional rendering of the liquid surface during the opening and closing of the orifice are shown in Figure 15 and in Figure 16, respectively. The end of the sequence in Figure 16 coincides with the orifice opening again, and with a new flow of fuel coming through the injection hole. The flow at these conditions is very rich in features and deserves further analysis in a following work.

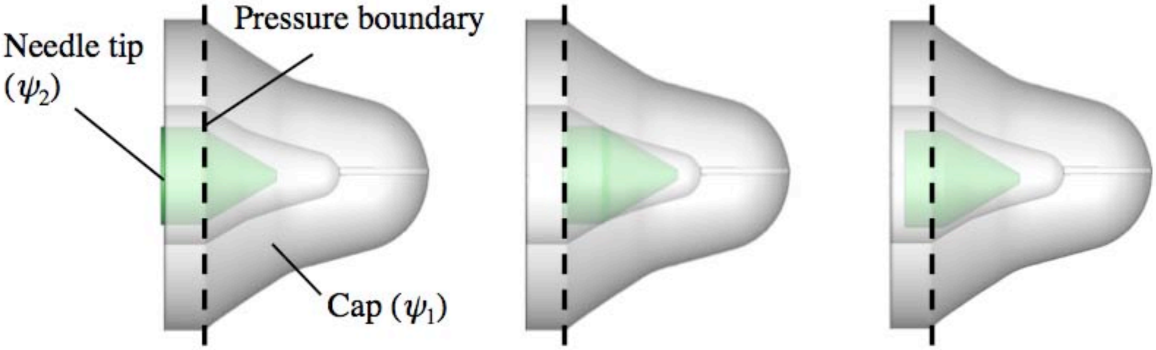

(a) (b) (c)

Figure 13. Relative motion of the two injector's components. The dashed line is the trace of the boundary plane in the simulation.

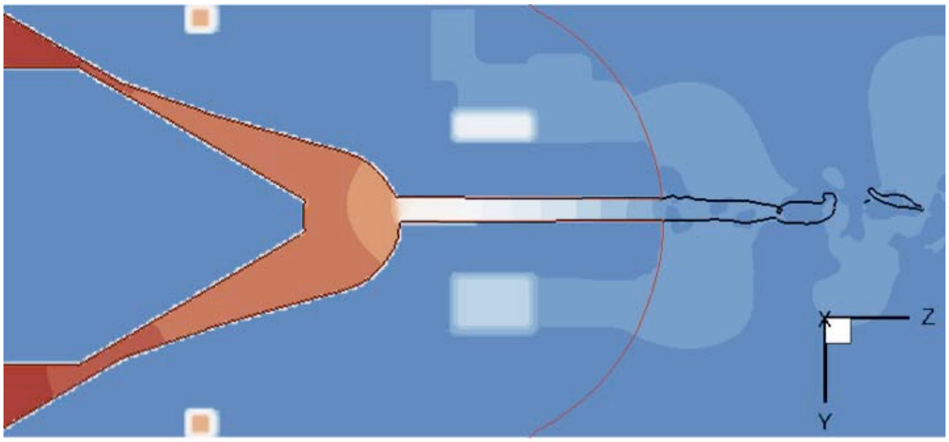

a) t = 1690 ms

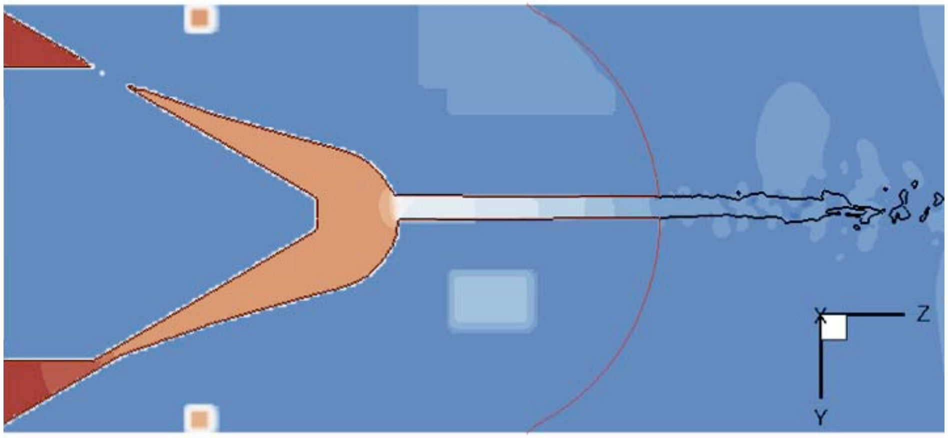

b) *t* = 1710 ms

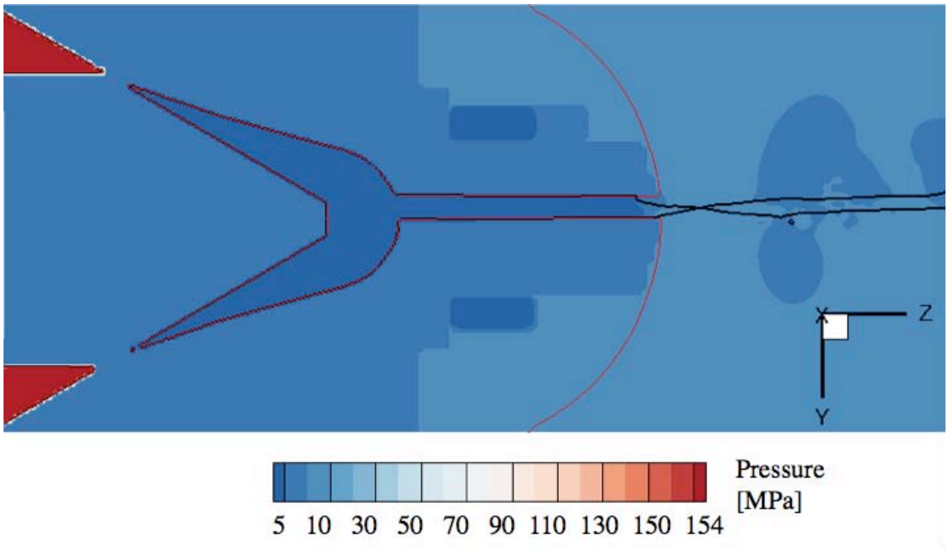

c) *t* = 1740 ms

Figure 14. Snapshots of plane sections through the injector axis. The black line is the intersection with the jet surface; the red line is the intersection with the solid wall.

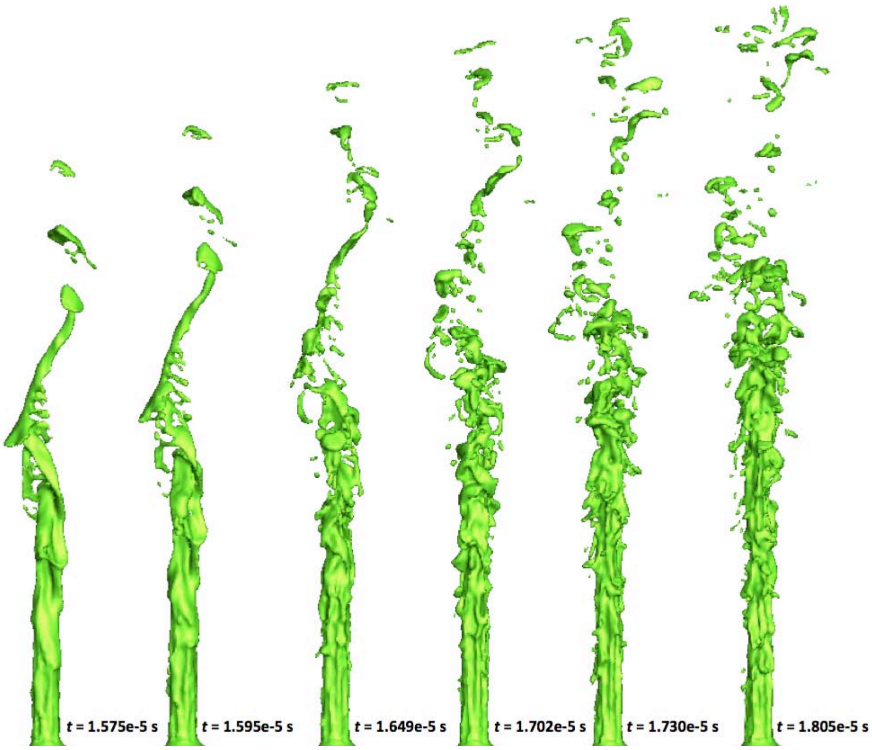

Figure 15. Orifice opening sequence.

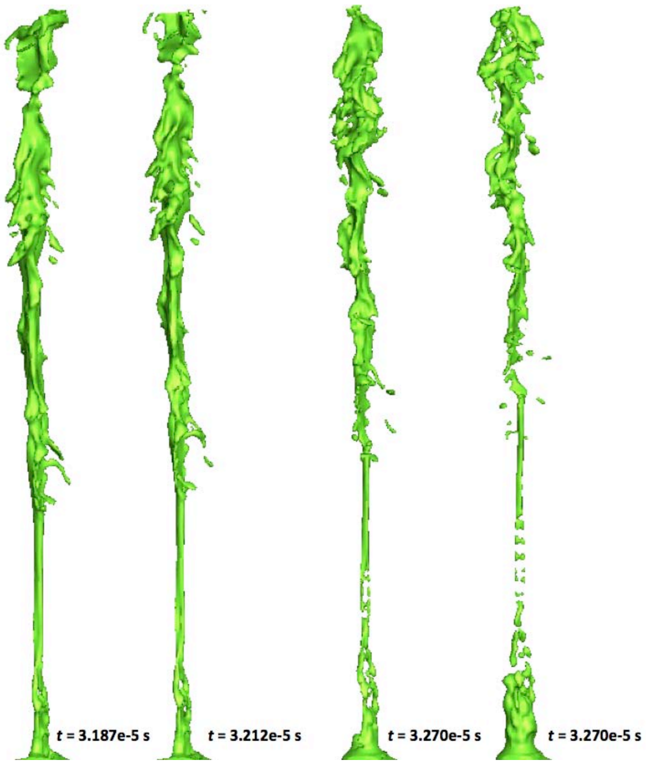

Figure 16. Orifice closing sequence.

3 MULTIPHASE COMPRESSIBLE CAPABILITY

In this Section, the multiphase capability for fuel injection simulation is extended to the compressible domain. This extension was carried out at Florida State University (Tallahassee, Florida) by Professor Sussman and his Ph.D. student Matthew Jamison. LDRD funding made it possible to follow their research and to execute a few computational tests related to liquid fuel injection: one of these tests is reported in detail here. The compressible, multiphase semi-implicit method is described in detail in [40], and only a few components related to the compressible formulation will be highlighted in the following.

It is important to point out that the interface reconstruction algorithm, CLSVOF, from Section 1 is now replaced by a more general multi-material methodology called Moment of Fluid (MOF). The MOF method tracks liquid volume fractions through advection, as does VOF, but uses the centroid of a material region (i.e., the first moment) inside a computational cell to determine the orientation of the interface [41]. The interface is chosen as the piece-wise linear reconstruction that exactly captures the volume fraction and minimizes error in the centroid. Centroid error can be interpreted as curvature in the interface, which ultimately is what should trigger adaptive mesh refinement. A description of the MOF method in the context of free-surface flow can be found in [42] together with the discussion of several computational tests (including a six-orifice injector simulation analogous to the one in Sec. 2.5).

A second difference with respect to the CLSVOF formulation is the concept of momentum-conserving projection to find velocities at cell faces [40]. The projection relies on the concept of departure region of a cell under advection. In Figure 17 the green region is solid, the yellow region is liquid, and the remainder is gas. The departure region Ω_D represents the forward-Euler approximation of the cell that is mapped to the cell enclosed by dashed purple lines (in this case, the control volume associated with a cell-face velocity). Ω_1 to Ω_4 are the intersection of the departure region with the control volumes.

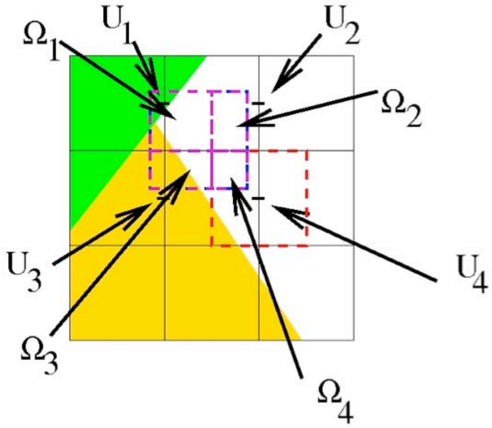

Figure 17. Illustration of semi-Lagrangian discretization for cell-face velocity.

3.1 Numerical model

In the multiphase, compressible formulation of the Navier-Stokes equations, density becomes a function of pressure and temperature as well. Momentum and mass conservation equations are written as

$$\frac{D(\rho(\phi)\mathbf{u})}{Dt} = -\nabla p + 2\nabla(\mu(\phi)\mathbf{D}) - \sigma\kappa\,\nabla H(\phi) \tag{20}$$

$$\rho_t + \nabla\cdot(\rho\mathbf{u}) = 0 \tag{21}$$

Pressure is evaluated according to the equation of state (EOS) for the fluid,

$$p = \mathrm{EOS}(e,\rho)\,, \tag{22}$$

where e is the internal energy.

For single-phase flow, Kwatra et al. [43] take advantage of the pressure evolution equation to alleviate the CFL condition imposed by the sound speed in simulating inviscid compressible flow with shocks, contacts and rarefactions. The pressure evolution equation

$$p_t + \nabla\cdot(\mathbf{u}p) = -\rho\, c^2 \nabla\cdot\mathbf{u} \tag{23}$$

can be derived from the mass conservation equation and from the material derivative $D\rho/Dt = \partial\rho/\partial t + \mathbf{u}\cdot\nabla\rho$,

$$\nabla\cdot\mathbf{u} = -\frac{1}{\rho}\frac{D\rho(s,p)}{Dt} = -\frac{1}{\rho}\left(\frac{\partial\rho}{\partial p}\right)_s \frac{Dp}{Dt} - \frac{1}{\rho}\left(\frac{\partial\rho}{\partial s}\right)_p \frac{Ds}{Dt} \quad . \tag{24}$$

This expression is equivalent to Eqn. (23) if we ignore the second term on the right-hand side of Eqn. (24) and recall that $c^2 = (\partial p/\partial\rho)_s$. Since pressure is not a conserved quantity, it is neither necessary nor physically relevant to use a conservative advection strategy. Intermediate, advected values $(\rho\mathbf{u})^a$ and $(\rho E)^a$, however, are calculated with a momentum-conservative strategy. E is the total energy, $E = e+1/2|\mathbf{u}|^2$. With these updated values, the pressure is updated following Eqn. (23):

$$p^{n+1} - (\rho c^2)^a \Delta t^2 \nabla\cdot\left(\frac{\nabla p^{n+1}}{\rho^{n+1}}\right) = p^a - (\rho\, c^2)^a \Delta t\ \nabla\cdot\mathbf{u}^a \tag{25}$$

On the left-hand side of Eqn. (25) we recognize a formulation of the Poisson's equation with variable coefficients. On the right-hand side, care must be taken in discretizing $\nabla\cdot\mathbf{u}^a$ using advective face velocities that are consistent with the pressure projection update of velocity; see [40] for details. After evaluating pressure at cell faces, the cell-averaged momentum and energy are updated

$$\frac{\rho_i^{n+1}\left(u_i^{n+1} - u_i^a\right)}{\Delta t} = -\frac{p_{i+1/2}^{n+1} - p_{i-1/2}^{n+1}}{\Delta x} \tag{26}$$

$$\frac{\rho_i^{n+1}\left(E_i^{n+1} - E_i^a\right)}{\Delta t} = -\frac{\left(p\ u\right)_{i+1/2}^{n+1} - \left(p\ u\right)_{i-1/2}^{n+1}}{\Delta x} \quad . \tag{27}$$

In the case of multiphase flow, wherever liquid and gas phases coexist in a computational cell Ω_j, this needs to be separated in a liquid (Ω_j^L) and gas (Ω_j^G) regions. Volume fractions are advected and the MOF reconstruction is performed in order to reconstruct the interfaces in the cell of interest. Mass is kept separate, therefore two equations must be solved for density.

$$\rho_j^{n+1,L} = \frac{\sum_{i'} \int_{\Omega_{i'}^L \cap \Omega^D} \rho_{i'}^{n,L}(x)\, d\Omega}{\int_{\Omega^L} d\Omega} \tag{28}$$

for the liquid phase and

$$\rho_j^{n+1,G} = \frac{\sum_{i'} \int_{\Omega_{i'}^G \cap \Omega^D} \rho_{i'}^{n,G}(x)\, d\Omega}{\int_{\Omega^G} d\Omega} \tag{29}$$

for the gas phase. Finally, any material in the simulation can be treated as compressible or incompressible or as a rigid body, as shown in the following example.

3.2 The Argonne experiment

A demonstration was carried out by replicating the conditions of the experiment reported in [44] by the Advanced Photon Source and Energy System Division at the Argonne National Laboratory in collaboration with Cornell University. Synchrotron x-radiography and a fast x-ray detector were used in the experiment to record the time evolution of fuel spray from a high-pressure injector. The diesel injection system was a high-pressure common-rail device that can be typically found in a passenger car, but with a specially fabricated single-orifice nozzle, 178 mm in diameter. The injection pressure was varied between 50 and 135 MPa. SF6, a heavy gas with molecular weight of 146, was used to replicate the relatively dense ambient gas environment during the adiabatic compression part of the engine cycle, when the diesel fuel is normally injected. The sonic speed in SF6 at room temperature is 136 m/s, considerably less than the 330 m/s speed of sound in air at the same conditions.

Published simulation results for the Argonne experiment have relied on the representation of the liquid phase with discrete Lagrangian parcels [46]. Similar to models developed for dilute sprays, each Lagrangian element, or parcel, represents several particles with identical fluid properties, such as velocity and temperature. However, since the interaction of a liquid element in the jet core with other liquid elements is in general different from the interaction of an isolated drop with the surrounding gas flow, such a Lagrangian parcel approach remains empirical in that the mass, momentum, and energy coupling terms between parcels and with the gas phase need to be carefully evaluated for each injection configuration.

A fully Eulerian approach to the calculation of supersonic injection is presented in [45]. This is an alternative approach where the multiphase flow is treated as a mixture supplemented with additional equations for the mass fraction of the mixture constituents. However, without explicitly solving for mass, momentum and energy equation for each phase, it becomes very challenging to model Eulerian closure terms in a manner that is consistent with the thermodynamics of the system, particularly the acoustic speed of the resulting homogenized multiphase system. In general, an equilibrium formulation must be assumed, so that the temperatures, pressures and velocities for both phases in the gas/liquid mixture are the same. The flow in [45] is treated as inviscid, whereas it has the correct viscosity (of liquid and gas) in the current simulation.

The results presented here were carried out using the all-speed capability coupled to the MOF interface-capturing technique. The total injection pressure reported for this case was 135 MPa and corresponded to a condition where the fuel jet velocity increased monotonically and always exceeded the sound speed in the gaseous phase. Because of the unavailability from [44] of the injector geometry, or even only the pressure drop measured across the device, a simple hollow cylinder was used to generate a pressure drop corresponding to the initial leading edge velocity of the jet (the cylinder is visible on the top left-hand side of Figure 18). The jet tip velocity, reported as a function of time in [46], was used to estimate the pressure drop. With a value at the start of injection of 200 m/s, the pressure boundary value was assigned to be 5 MPa in the simulation.

The computational domain was reduced to a quarter by imposing symmetry conditions at two orthogonal planes passing by the injector's axis. Outflow boundary conditions were set on the remaining domain boundaries. The computational domain measured 2 cm in the axial direction of injection and 1 by 1 cm in the transverse direction. The base level consisted of 32×32×64 computational cells, with six levels of refinement. At run time, cells were tagged for refinement according to two distinct criteria: liquid volume fraction above a 0.05 threshold; or local pressure gradient sufficiently steep. In this way, the liquid surface and the leading shock wave could both be resolved with the maximum available grid density. A snapshot of the adaptive grid taken at the same instant of Figure 18 is shown in Figure 19. One can easily track the location of the leading shock as well as the main body of the jet. Each level of refinement is composed by up to a few thousand grid blocks. Each grid block had maximum grid size of 64 cells. The coverage efficiency, that is, the ratio of cells meeting the refinement criteria to the cells eventually tagged for refinement, was 0.90. The simulation shows long ligaments, but only a limited amount droplets surrounding the jet. The simulation proceeded by calculating the stable time interval at each step. To capture in a time-resolved manner the leading shock in the gas phase, both sound speed and flow velocity were used to estimate the time interval, whereas only the flow velocity (and not the much larger sound speed) was used for the liquid phase. As a result, after an initial transient where Δt decreased to 10^{-10} s, the time step eventually stabilized at around $2 \cdot 10^{-9}$ s.

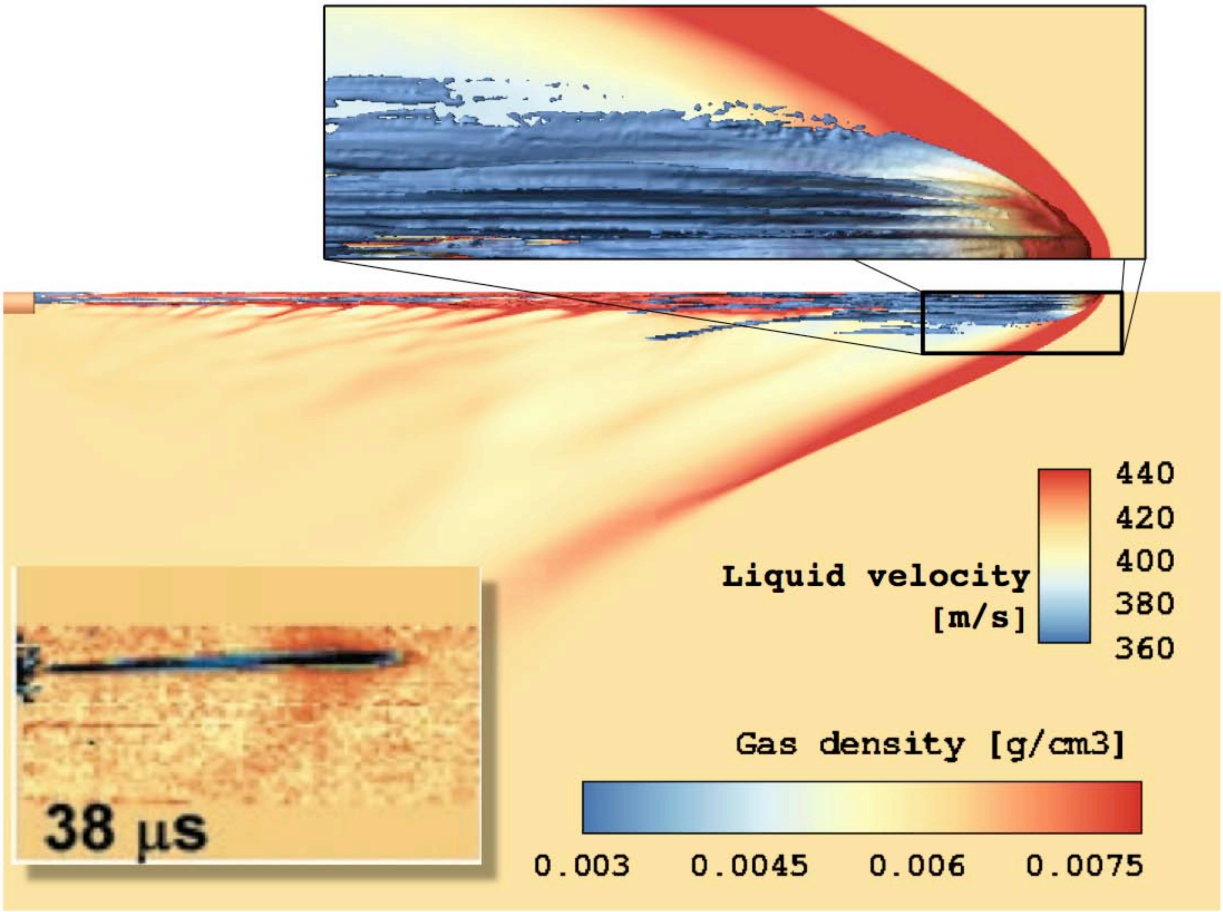

Figure 18. Simulation snapshot at 38 ms from injection with contour plot of the gas density saturated at 0.0075 g cm^{-3} to highlight the leading edge oblique shock wave and a system of weaker compression waves neat the liquid jet. The insert at the top of the figure shows the surface of the jet tip, colored by velocity. The simulation snapshot is compared at the same instant with the average of 20 x-radiography images from distinct fuel injection cycles (in the bottom right-hand side insert). The false-color levels of x-radiography were set to accentuate small differences in the x-ray intensity arising from the slightly increased x-ray absorption in the compressed gas.

In examining the density plot in Figure 18, one can also notice oblique waves propagating from the body of the jet. A similar pattern can be observed in one optical Schlieren image from [44], although in a different configuration and condition than in the simulation. The Schlieren image displays a broad, dark region near the jet leading edge. This region corresponds to the optically dense cloud of droplets surrounding the thin, main fuel jet. This is obviously only a demonstration simulation that requires further verification and validation tests before carrying out an in-depth study of the features of the jet core.

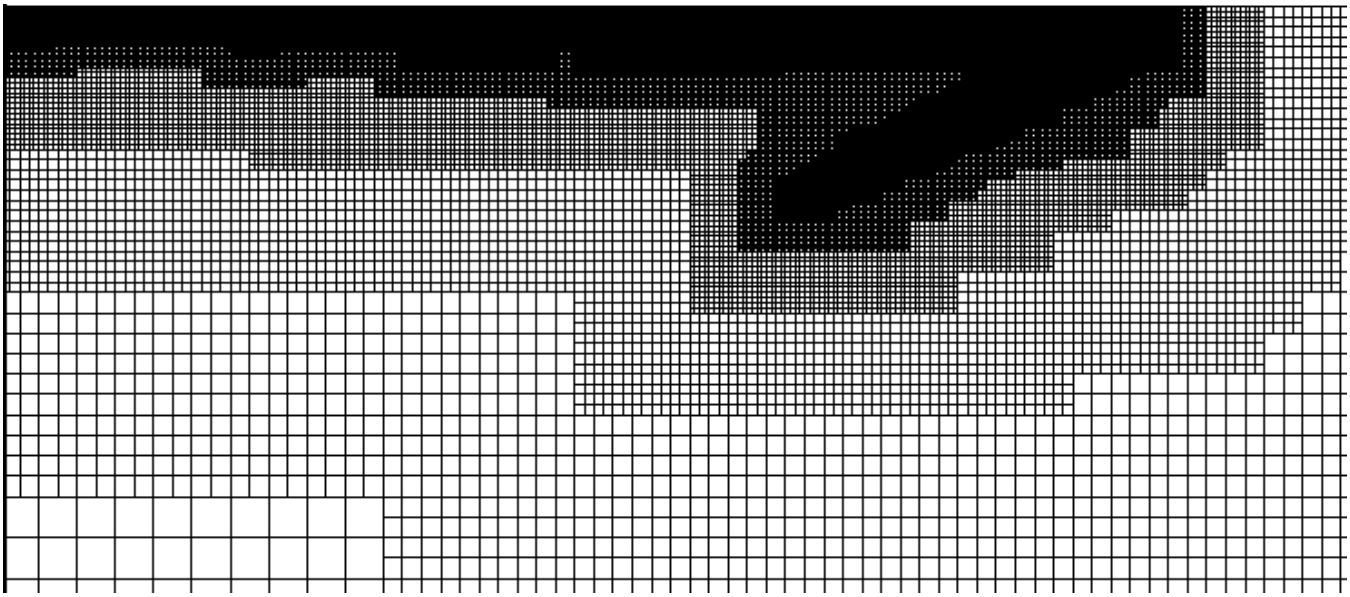

Figure 19. Superimposed levels of refinement on one side of the computational domain at the time corresponding to Figure 18.

4 CONCLUSION

In this LDRD project, a new simulation capability was developed where internal and external flows can be calculated seamlessly across an injection orifice. The external liquid-gas interface is handled by the combined level-set volume-of-fluid (CLSVOF) method and the solid wall boundary is represented by a different level-set function on the same block-structured grid. This approach shifts the burden of handling complex internal geometries to the much simpler task of obtaining a tessellation of the injector surfaces, therefore sidestepping volume mesh generation altogether.

The numerical technique for handling solid boundaries belongs to the group of Cartesian grid methods with embedded boundaries, but the capability to model at the same time liquid jet formation and free-surface turbulence is unique. Moving parts of the injector and contacts, such as they occur when the needle shifts during operation cycle, are trivial to include because they simply require a level-set recalculation. The accuracy of the embedded boundary method appears to be at best first-order accurate, but improvements can be borrowed from other methods, mostly single-phase, at the price of increased implementation complexity.

In the last part of the project, this multiphase capability was extended to compressible flow. The new algorithm uses a semi-implicit pressure update scheme that asymptotically preserves the standard incompressible pressure projection method in the limit of infinite sound speed. This attribute makes the new method applicable to compressible and incompressible flows, while allowing for larger time steps than the standard explicit CFL restriction. Shocks are captured and material discontinuities are tracked, without the aid of any approximate or exact Riemann solver. An example relevant to Diesel injection is presented at the end of the report. This new capability opens many new modeling opportunities in multiphase applications where compressibility plays a big role.

Further work will address issues associated with internal flow in real-size injectors, such as cavitation and liquid phase compressibility. The most outstanding challenge remains the essential “stiffness” of this class of problems, that is, the injection physics requires the stable timestep to be several orders of magnitude smaller than the full injection cycle time.

During the course of this project, a few opportunities have emerged, sometimes outside the automotive field, that directly leverage on the capabilities developed in the past two years:

- A new LDRD project was awarded in 2012 by the Geo-Science Foundation to study the scattering properties of atmospheric aerosol ($245k/year for three years). Key simulations are expected to be carried out with CLSVOF.

- An LDRD proposal in Engineering Science ($500k/year for three years) was down-selected in 2013: the decision on the final awards is pending at this moment. The project concerns the development of a Large Eddy Simulation framework for primary atomization. Because of the diagnostics’ difficulties in accessing the near-injection region, CLSVOF will provide “truth” simulations that will be used for model development.

- An exploratory study on fiber manufacturing processes for polymers will begin in Summer 2013 with $38k in funding: the capability of maintaining a sharp liquid-gas interface at very large gas velocities (even supersonic) was considered a unique asset for modeling this complex manufacturing process. Collaborations to explore the behavior of molten metals in highly turbulent gas flow are under consideration.

5 REFERENCES

1. Benjamin, M.A., Jensen, R.J., Arienti, M. *Review of Atomization: Current Knowledge and Future Requirements for Propulsion Combustors*, Atomization and Sprays (2010) vol. 20(6) pp. 485–512.
2. Sussman, M., Smith, K., Hussaini, M. Y. Ohta, M., Wei, R.-Z. *A Sharp Interface Method for Incompressible Two-Phase Flows*, Journal of Computational Physics (2007) 469-505.
3. CCSE 2012. https://ccse.lbl.gov/BoxLib/index.html
4. Li, X., Arienti, M., Soteriou, M., and Sussman, M., *Towards an Efficient, High-Fidelity Methodology for Liquid Jet Atomization Computations*, 48th AIAA Aerospace Sciences Meeting 2010, AIAA Paper 2010-0210, 2010.
5. http://www.math.fsu.edu/~sussman/
6. Arienti, M., Li, X., Soteriou, M.C., Eckett, C.A., Sussman, M., and Jensen, R. J. *Coupled Level-Set/Volume-of-Fluid Method for Simulation of Injector Atomization*. Journal of Propulsion and Power, 29(1):147-157, 2013.
7. Stewart, P. A., Lay N., Sussman, M. and Ohta M., 2008. An Improved Sharp Interface Meth-od for Viscoelastic and Viscous Two-Phase Flows. J. of Scientific Computing, 35(1), 43-61.
8. Sussman, M., and Ohta, M., 2009. *A Stable and Efficient Method for Treating Surface Tension.* SIAM J. Sci. Comput. 31(4): 2447-2471.
9. Sussman, M. and Dommermuth, D., 2001. *The numerical simulation of ship waves using Cartesian grid methods. Proceedings of the 23rd Symposium on Naval Ship Hydrodynamics*, Nantes, France, 762–779.
10. Kadiouglu, S. Y. and Sussman, M., 2008. *Adaptive Solution Techniques for Simulating Underwater Explosions and Implosions.* J. of Comp. Phys. 227:2083-2104.
11. Li, X., Arienti, M., Soteriou, M., and Sussman, M., 2010. *Towards an Efficient, High-Fidelity Methodology for Liquid Jet Atomization Computations*. AIAA-2010-0210, 48th AIAA Aerospace Sciences Meeting 2010.
12. Arienti, M., Li, X., Soteriou, M. C., Eckett, C. A., Sussman, M., and Jensen, R. J. *Coupled Level-Set/Volume-of-Fluid Method for Simulation of Injector Atomization.* Journal of Propulsion and Power, Vol. 29(1): pp. 147-157 (2013).
13. Ménard, T., Tanguy, S. and Berlemont, A., 2007. *Coupling level set/VOF/ghost fluid methods: Validation and application to 3D simulation of the primary break-up of a liquid jet*. Int. J. of Multiphase Flow 33 510-524.
14. Herrmann, M., 2010. *Detailed Numerical Simulations of the Primary Atomization of a Turbulent Liquid Jet in Crossflow*. ASME J. Eng. Gas Turb. Power, 132(6), 061506.1-10.
15. Aftosmis, M. J., Berger, M. J., and Melton, J. E., 1997. *Robust and Efficient Cartesian Mesh Generation for Component-Based Geometry*. AIAA Paper 97-0196.
16. Arienti, M., Hung, P., Morano, E. and Shepherd, J. E. 2003. *A level set approach to Eulerian–Lagrangian coupling*. J. Comp. Phys. 185:213-251.
17. Berger, M. J. and LeVeque, R., 1990. Stable Boundary Conditions for Cartesian Grid Calculations. Symposium on Computational Technology for Flight Vehicles, Pergamon Press.

18. Bayyuk, S.A., Powell, K.G., and van Leer, B., 1993. *A Simulation Technique for 2-D Unsteady Inviscid Flows around Arbitrarily Moving and Deforming Bodies of Arbitrary Geometry*. AIAA Paper 93-3391-CP.
19. Peskin, C. S., 1972. *Flow Patterns Around Heart Valves: a Numerical Method*, J. Comput. Phys. 10 252-271.
20. Yang, J. and Balaras, E., 2006. *An Embedded-Boundary Formulation for Large-Eddy Simulation of Turbulent Flows Interacting with Moving Boundaries.* J. Comput. Phys. 215:12-40.
21. Baer, T. A., Cairncross, R. A., Schunk, P. R., Rao, R. R., and Sackinger P. A., 2000. *A Finite Element Method for Free Surface Flows of Incompressible Fluids in Three Dimensions. Part II. Dynamic Wetting Lines.* Int. J. for Numerical Methods in Fluids 33:405-427.
22. Liu, H., Krishnan, S., Marella, S., Udaykumar, H. S. 2005. *Sharp interface Cartesian grid method II: a technique for simulating droplet interactions with surfaces of arbitrary shape*. J. Comput. Phys. 210: 32-54.
23. Krishnan, S., Liu, H., Marella, S., and Udaykumar, H. S. 2006. *A Sharp-Interface Cartesian Grid Method for Computations of Droplet Impact and Spreading on Surfaces of Arbitrary Shape*, IUTAM Symposium on Computational Approaches to Multiphase Flow Fluid Mechanics and Its Applications 81:293-300.
24. Yang, J. and Stern, F., 2009. *Sharp interface immersed-boundary/level-set method for wave–body interactions*. J. Comput. Physics 228:6590-6616.
25. Afkhami, S. and Bussmann, M., 2009. *Height Functions for Applying Contact Angles to 3D VOF Simulations*, Int. J. Numer. Meth. Fluids 61(8):827-847.
26. Noël, E., Berlemont, A., Cousin, J. and Ménard, T., 2012. *Application of the Immersed Boundary Method to Simulate Flows Inside and Outside the Nozzles.* ICLASS 2012, 12th Triennial International Conference on Liquid Atomization and Spray Systems, Heidelberg, Germany, September 2-6.
27. Arienti, M., and Sussman, M., 2012. *Nozzle geometry Effects on Primary Atomization.* ICLASS 2012, 12th Triennial International Conference on Liquid Atomization and Spray Systems, Heidelberg, Germany, September 2-6.
28. Arcoumanis, C., Gavaises, M., Nouri, J. M., Abdul-Wahab, E., Horrocks, R. W., 1998. *Analysis of the Flow in the Nozzle of a Vertical Multi-Hole Diesel Engine Injector*. SAE Technical Series 980811.
29. Kastengren, A. L., Tilocco, F. Z., Powell, C. F. Manin, J., Pickett, L. M., Payri, R., and Bazyn, T. *Engine Combustion Network (ECN): Measurements of Nozzle Diameter and Hydraulic Behavior of Diesel Sprays*. To appear in Atomization and Sprays.
30. Chang, Y.C., Hou T.Y., Merriman, B., and Osher, S., 1996. *A Level Set Formulation of Eulerian Interface Capturing Methods for Incompressible Fluid Flows.* J. Comput. Phys. 124: 449-464.
31. Sussman, M., Smith, K. M., Hussaini, M. Y., Ohta M. and Zhi-Wei, R., 2007. *A Sharp Interface Method for Incompressible Two-Phase Flows*, J. Comput. Phys. 221(2): 469-505.
32. Mauch, S., 2000. *A Fast Algorithm for Computing the Closest Point and Distance Transform.* Caltech Technical Report caltechASCI/2000.077.
33. CCSE 2012. https://ccse.lbl.gov/BoxLib/index.html

34. Duffy, A., Kuhnle, A. and Sussman M. *An Improved Variable Density Pressure Projection Solver for Adaptive Meshes.* Preprint at http://www.math.fsu.edu/~sussman/MGAMR.pdf
35. Dennis, S. C. R., and Chang, G.-Z., 1970. *Numerical solutions for steady flow past a circular cylinder at Reynolds numbers up to 100.* J. Fluid Mech. 42: 471-489.
36. Calhoun, D., 2002. *A Cartesian Grid Method for Solving the Two-Dimensional Streamfunction-Vorticity Equations in Irregular Regions.* J. Comput. Phys. 176: 231-275.
37. Seo, J. H. and Mittal, R., 2011. *A Sharp-Interface Immersed Boundary Method with Improved Mass Conservation and Reduced Spurious Pressure Oscillations*, J. Comp. Phys. 230:7347–7363.
38. Dütcsh, H., Durst, F., Becker, S., and Lienhart, H., 1980. *Low-Reynolds-Number Flow Around an Oscillating Circular Cylinder at Low Keulegan-Carpenter Numbers*. J. Fluid Mech. 360:249-271.
39. ECN 2013. http://www.sandia.gov/ecn/cvdata/targetCondition/injectorNozGeom.php
40. Jemison, M., Sussman, M., Shashkov, M., and Arienti, M. *Compressible, Multiphase Semi-Implicit Method with Moment of Fluid Interface Representation.* In preparation.
41. Dyadechko, V., and Shashkov, M. *Moment-of-fluid interface reconstruction*. Technical report, Los Alamos National Laboratory, Oct 2005. Available online at http://math.lanl.gov/vdyadechko/doc/2005-mof.pdf, 2005.
42. Jemison, M., Loch, E., Sussman, M., Shashkov, M., Arienti, M., Ohta, M., and Wang, Y. *A coupled level set-moment of fluid method for incompressible two-phase flows*. J. Sci. Comput., 54(2-3):454–491, Feb. 2013.
43. Kwatra, N., Su, J., Grétarsson, J.T., Fedkiw, R., *A Method for Avoiding the Acoustic Time Step Restriction in Compressible Flow*, Journal of Computational Physics 228 (2009) 4146-4161.
44. MacPhee, A.G., et al., *X-ray Imaging of Shock Waves Generated by High-Pressure Fuel Sprays*, Science 295, 1261 (2002); DOI: 10.1126/science.1068149
45. Lagumbay, R.S., Vasilyev, O.V., Haselbacher, A., and Wang, J., *Numerical Simulation of a High Pressure Supersonic Multiphase Jet Through a Gaseous Medium*. Proceeding of IMECE’04, 2004 ASME International Mechanical Engineering Congress Expo, Anaheim, California, Nov. 13-19, 2004. IMECE2004-61008
46. Im, K-S et al., *Interaction between Supersonic Disintegrating Liquid Jets and Their Shock Waves*, Physical Review Letters, 102, 074501 (2009).

DISTRIBUTION

1	MS 9054	Art Pontau	8360 (electronic copy)
1	MS 9957	Greg Wagner	8365 (electronic copy)
1	MS 0836	John Hewson	1532 (electronic copy)
1	MS0899	Technical Library	9536 (electronic copy)
1	MS0359	D. Chavez, LDRD Office	1911

Sandia National Laboratories
